nature portfolio

https://doi.org/10.1038/s41586-026-10587-4

Supplementary information

Continuously graded-doped SnO_2 for efficient n–i–p perovskite solar cells

In the format provided by the authors and unedited

Supplementary Information for

Continuously graded-doped SnO_2 for efficient n–i–p perovskite solar cells

Di Wang (王迪)[1†], Saisai Li (李赛赛)[1†], Zijin Ding (丁紫津)[1†], Jian Xu (徐健)[2*], Xingyu Chen (陈星宇)[1], Qiao Zheng (郑樵)[1], Thamraa Alshahrani[3], Siyu Liu (刘思宇)[9], Tingwei He (何庭伟)[8], Xinxin Yue (岳鑫欣)[7], Saif M. H. Qaid[5], Keyu Wei (韦科妤)[1], Xuewen Fu (付学文)[7], Lin Feng (冯林)[4], Ou Yang (杨欧)[4], Huanxin Ju (鞠焕鑫)[4], Yuanzhi Jiang (姜源植)[1,6*], Jun Chen (陈军)[1,6], Mingjian Yuan (袁明鉴)[1,6*]

[1]*State Key Laboratory of Advanced Chemical Power Sources, Frontiers Science Center for New Organic Matter, Key Laboratory of Advanced Energy Materials Chemistry (Ministry of Education), Academy for Advanced Interdisciplinary Studies, College of Chemistry, Nankai University; Tianjin, P. R. China.*

[2]*School of Interdisciplinary Science, Beijing Institute of Technology; Beijing, P. R. China.*

[3]*Department of Physics, College of Science, Princess Nourah Bint Abdulrahman University; Riyadh, Saudi Arabia.*

[4]*PHI Analytical Laboratory, ULVAC-PHI Instruments Co.,Ltd; Nanjing, P. R. China.*

[5]*Department of Physics & Astronomy, College of Science, King Saud University; Riyadh, Saudi Arabia.*

[6]*Haihe Laboratory of Sustainable Chemical Transformations; Tianjin, P. R. China.*

[7]*Ultrafast Electron Microscopy Laboratory, The MOE Key Laboratory of Weak-Light Nonlinear Photonics, College of Physics, Nankai University; Tianjin, P. R. China.*

[8]*College of Physics Science and Technology, Hebei University; Baoding, Hebei, P. R. China.*

[9]*Nano-Science Center and Department of Chemistry, University of Copenhagen; Copenhagen, Denmark.*

[†]These authors contributed equally to this work.

*Corresponding authors. Emails: yuanmj@nankai.edu.cn; jianxu.xu@bit.edu.cn; yz.jiang@nankai.edu.cn

Contents

Supplementary Note 1 | Quantitative analysis of contact loss for n–i–p devices.

We fabricated n-i-p configuration devices using TGA-capped SnO_2 ETLs (denote TGA-SnO_2 or control-SnO_2), delivering a champion efficiency of 26.01% (**Extended Data Fig. 2**). Statistical data collected from 20 independent devices were plotted in **Supplementary Fig. 1**, exhibiting a substantial V_{oc} loss exceeding 340 mV, and *FF* below 84%.

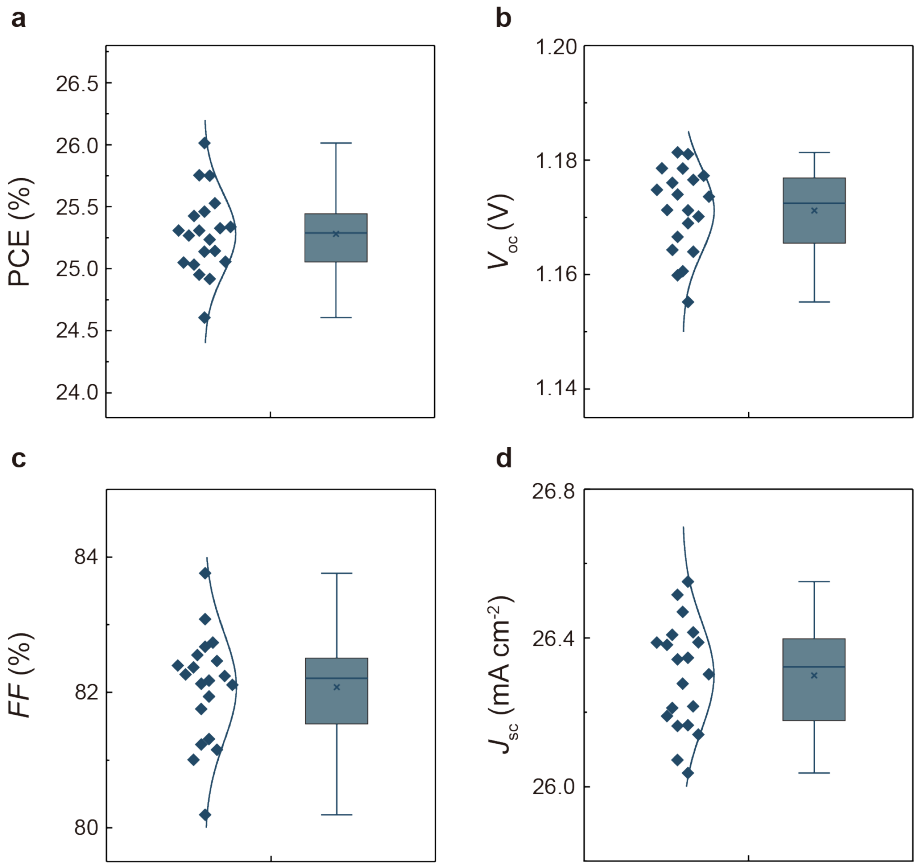

Supplementary Fig. 1 Statistics of PCE (**a**), V_{oc} (**b**), *FF* (**c**), J_{sc} (**d**) for the devices based on control-SnO_2.

To elucidate the origin of these losses, we conducted photoluminescence quantum yield (PLQY) measurements on neat perovskite, ETL/perovskite, and perovskite/HTL stacks, respectively. As shown in **Supplementary Fig. 2**, once the perovskite contacted with TGA-SnO_2 ETL, a substantial PLQY decrement was observed, indicating significant nonradiative recombination occurred at the TGA-SnO_2 ETL/perovskite interface. We then extracted the *quasi*-Fermi level splitting

(QFLS) using equations 1-3, which revealed a 36 meV reduction in QFLS at the buried interface compared to neat perovskite film.

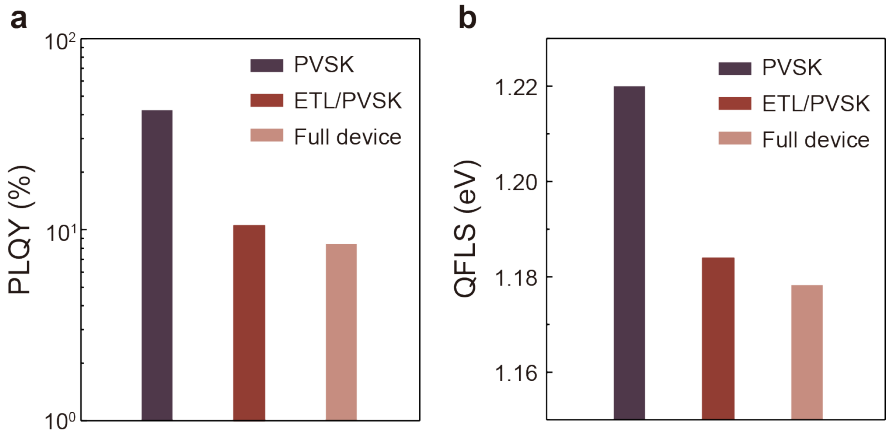

Supplementary Fig. 2 a, PLQY measurements for neat perovskite, perovskite with ETL stack, and full device. **b**, Calculated QFLS of stacks from PLQY data.

QFLS was calculated by following equations:

$$QFLS = QFLS_{rad} + k_B T \ln(PLQY) = k_B T ln\left(PLQY \frac{J_G}{J_{0,rad}}\right) \quad 1$$

where k_B is the Boltzmann constant, and T is the temperature (300 K). J_G represents the current density generated under 1 sun equivalent illumination, approximated to device's short-circuit current density J_{sc}. $J_{0,rad}$ is the radiative recombination current density in the dark condition.

$J_{0,rad}$ can be calculated according to the detailed balance:

$$J_{0,rad} = e \int_0^\infty EQE_{PV}(E) \Phi_{BB}(E) dE \quad 2$$

$$\Phi_{BB}(E) = \frac{2\pi E^2}{h^3 c^2} \frac{1}{\exp\left(\frac{E}{k_B T}\right) - 1} \quad 3$$

where EQE_{PV} is the external quantum efficiency of device, h is the Planck constant, c is the speed of light in vacuum.

Supplementary Note 2 | Origin of contact loss at CBD SnO_2/perovskite buried interface.

1. Conduction band minimum (CBM) misalignment.

UPS and UV-vis characterizations revealed a large conduction band offset (~300 meV) at the TGA-SnO_2/perovskite interface (**Supplementary Fig. 3**, **Supplementary Table 1**).

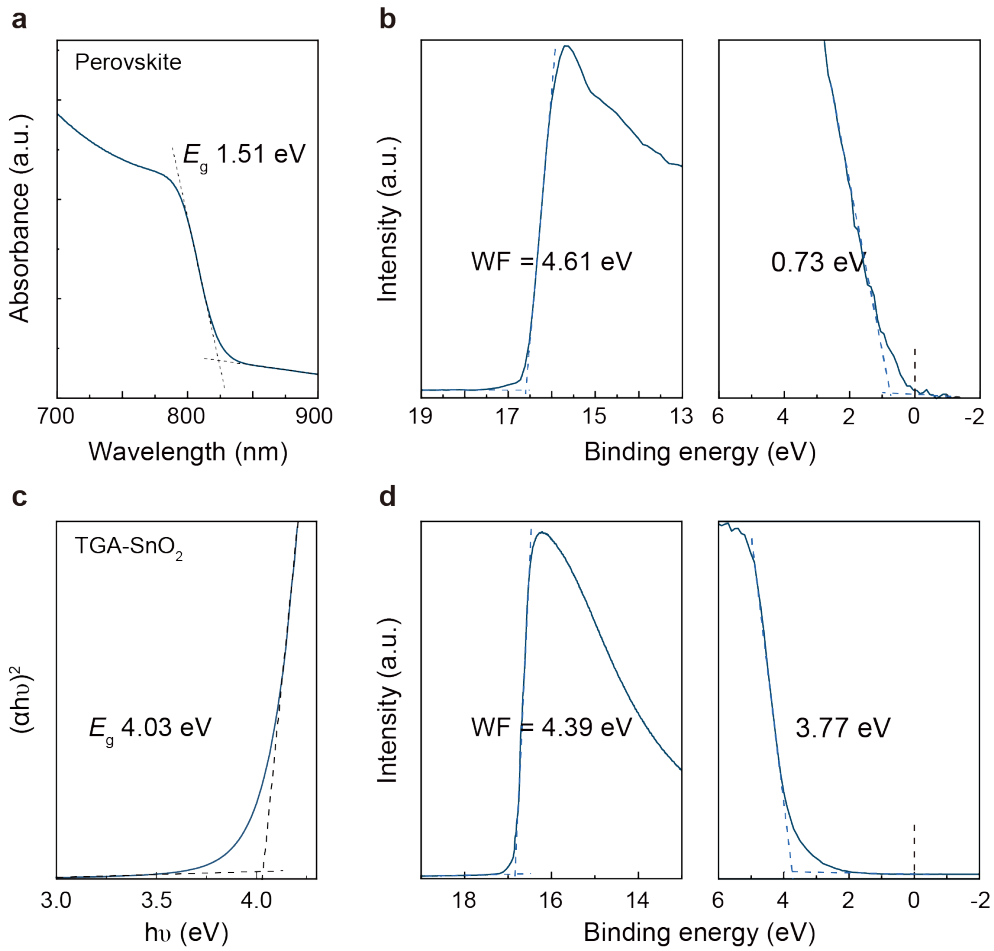

Supplementary Fig. 3 UV-vis absorption (**a**), secondary electron cut-off region and valence photoemission spectra of UPS spectra for perovskite (**b**). Tauc plot derived from UV-vis spectrum (**c**), secondary electron cut-off region and valence photoemission spectra of UPS spectra for TGA-SnO_2 (**d**).

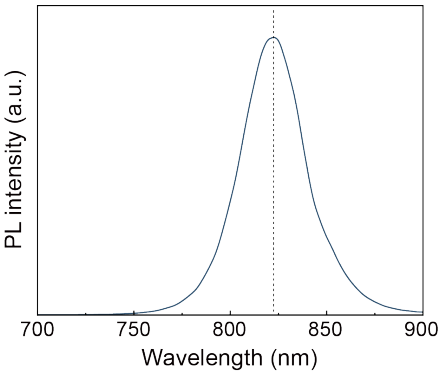

Supplementary Fig. 4 PL spectrum for perovskite absorber.

2. Sluggish electron extraction.

To probe the charge extraction dynamics, we performed TRPL spectra on neat perovskite, ETL/perovskite, perovskite/HTL stacks, respectively. Using the lifetime of the fast decay process as an indicator of charge extraction (**Supplementary Fig. 5**), we found that the perovskite/HTL stack exhibited a notably shorter τ_1 of 2.5 ns compared to 24.7 ns for the TGA-SnO_2/perovskite stack, indicating a pronounced extraction imbalance. To further quantify this behavior, we calculated the electron-transfer rate (k_{ET}) and extraction efficiencies η for both interfaces in **Supplementary Table 4**[1-4]. The k_{ET} and η for TGA-SnO_2/perovskite (1.15×10^7 s^{-1} and 97.14%, respectively) were quantitively lower than those for the perovskite/HTL (4.27×10^7 s^{-1} and 99.21%). Collectively, these results demonstrated a charge extraction imbalance between electron and hole at the buried TGA-SnO_2/perovskite interface, which in turn led to electron accumulation[6], thereby aggravating nonradiative recombination losses.

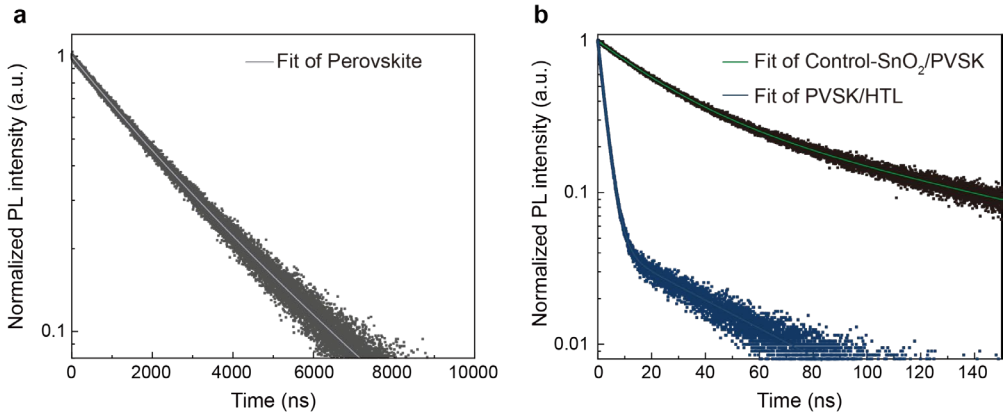

Supplementary Fig. 5 TRPL spectra of neat perovskite (**a**), control-SnO_2/perovskite and perovskite/HTL stacks (**b**).

To distinguish the origin of these losses, we carried out space-charge-limited current (SCLC) measurements on electron-only devices (**Supplementary Fig. 6)**, revealing that the defect density of TGA-SnO_2 ETL was similar to that of the currently optimized commercial SnO_2 (Alfa-SnO_2) with KCl passivation[5], which is known to exhibit low defect density. This similarity likely arises from *in-situ* passivation of vacancies and dangling bonds on the SnO_2 surface *via* ligands coordination during the CBD process. These results further supported that the nonradiative recombination loss primarily arises from the suppressed electron extraction, rather than defect-dominated non-radiative recombination.

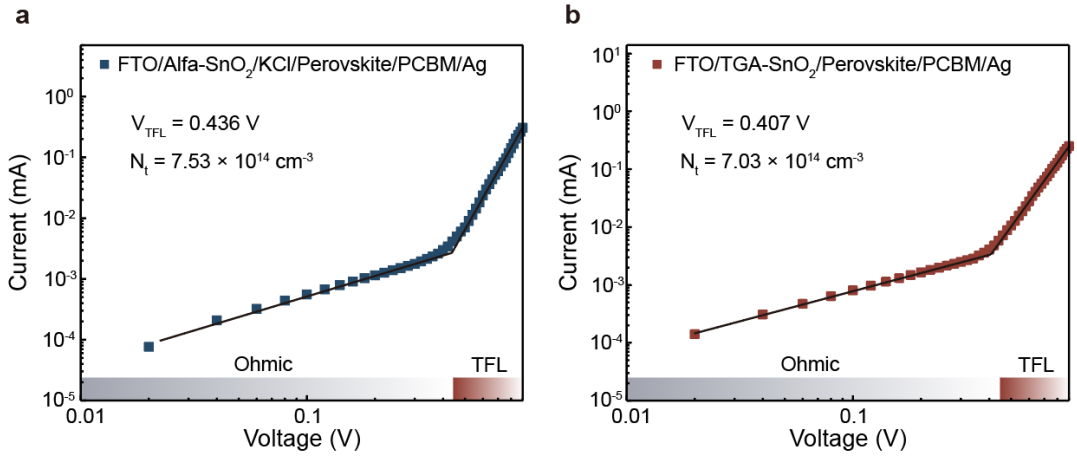

Supplementary Fig. 6 SCLC curves for the electron-only device based on Alfa-SnO_2 with KCl passivation (**a**), and TGA-SnO_2 (**b**).

The density of defect states (N_t) was linearly proportional to the onset voltage of a rapid nonlinear trap-filled limit rise (V_{TFL}).

$$N_t = \frac{2\varepsilon_0\varepsilon_r V_{TFL}}{qL^2} \quad 4$$

where ε_r is the relative dielectric constant, ε_0 is the vacuum permittivity, L is the film thickness.

Furthermore, we confirmed that the electron-hole extraction imbalance in TGA-SnO_2-based device was attributed to the strongly suppressed electron mobility of the TGA-SnO_2 ETL, compared with the hole mobility of the Spiro-OMeTAD HTL (**Supplementary Fig. 7**), which in turn lead to electron accumulation at the buried

interface.

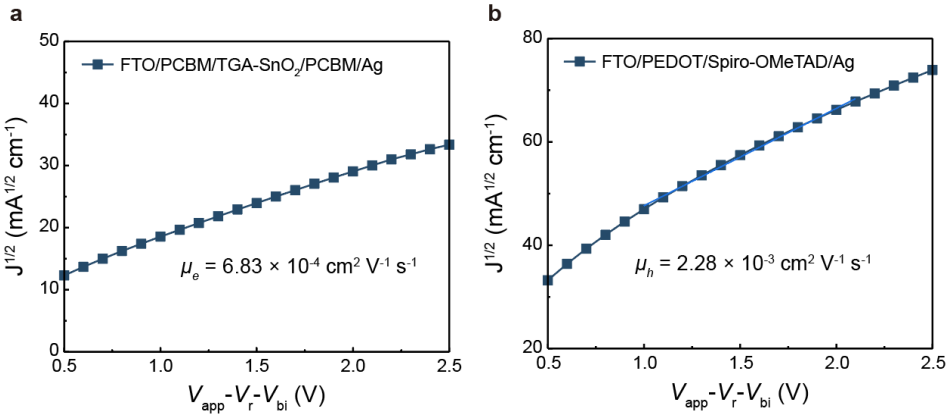

Supplementary Fig. 7 SCLC measurements for calculating the electron mobility calculation of TGA-SnO_2 ETL (**a**), and hole mobility calculation of Spiro-OMeTAD HTL (**b**), respectively.

The mobility (μ) of electron and hole were extracted by fitting the *J-V* curves using the Mott-Gurney law:

$$\mu_e = \frac{8JL^3}{9\varepsilon\varepsilon_0(V_{app} - V_r - V_{bi})^2} \quad 5$$

where J is the current density, L represents the thickness of the ETL and HTL, ε_0 is the vacuum permittivity, ε_r is the dielectric permittivity of the ETL and HTL, V_{app} refers to the applied voltage, V_r is the voltage loss caused by radiative recombination, and V_{bi} is the built-in voltage resulting from the different work function between the anode and cathode.

Supplementary Note 3 | Colloidal SnO_2 NPs assembly through electrostatic adsorption.

1. *Quasi*-layer-by-layer (*quasi*-LBL) deposition.

The SnO_2 ETL deposited *via* CBD process consists of uniformly stacked nanoparticles with sizes of 3-5 nm, rather than forming a continuous, homogeneous layer, as shown in **Extended Data Fig. 3**. Correspondingly, the film thickness increases monotonically with deposition time, indicating a growth process governed by the successive stacking of nanoparticle layers. We therefore defined this growth mode as "*quasi*-layer-by-layer", reflecting its hybrid nature that combines the ordered stacking characteristic of conventional LBL processes with the discrete nanoparticle architecture inherent to colloidal assembly.

2. Electrostatic assembly.

We systematically investigated the critical role of ligands by screening a series of thiol-based variants. To ensure high conductivity of SnO_2 film, we employed the short carbon-chain linker with thiol (-SH) as the head group, which exhibited strong coordination with tin, including monodentate ligand 2-mercaptoethane (ET), and bidentate ligands 2-mercaptoethylamine (TA), 2-mercaptoacetic acid (TGA), and 2-mercaptoethanol (TE) (**Extended Data Fig. 4**).

SEM and cyclic voltammetry (CV) characterization (**Extended Data Fig. 4c** and **4e**) revealed that only the carboxyl-terminated group yield a dense film. To understand the underlying selectivity, we conducted zeta potential measurements (**Extended Data Fig. 4d**). We found that under strongly acidic conditions (pH = 1.5-3), $-NH_2$ tail group tended to protonate into positively charged ammonium salt, while hydroxyl group remained protonated due to their high pK_a. Therefore, SnO_2 NPs capped with ligands with alkyl, amino, or hydroxyl groups tail groups carried a net positive surface charge, given the isoelectric point of SnO_2 (~5.5-6.0)[7]. This positive charge hindered NPs assembly onto FTO substrates, yielding nearly bare FTO surfaces after deposition.

In contrast, tail group with low pK_a, such as carboxyl-terminated, readily

deprotonated under acidic conditions to generate negatively charged colloidal NPs. This negative charge drove electrostatic adsorption onto the FTO substrate[7], enabling the formation of dense films.

Based on these findings, the deposition mechanism of CBD-SnO_2 films on FTO substrates can be summarized in two primary stages: (1) nucleation and growth of colloidal NPs in solution, mediated by ligand-capped slow hydrolysis of Sn^{2+} under conditions of steadily increasing pH induced by the gradual thermal decomposition of urea, together with oxidation by dissolved oxygen, and dehydration; and (2) *quasi*-layer-by-layer self-assembly of pre-formed colloidal NPs onto the substrate.

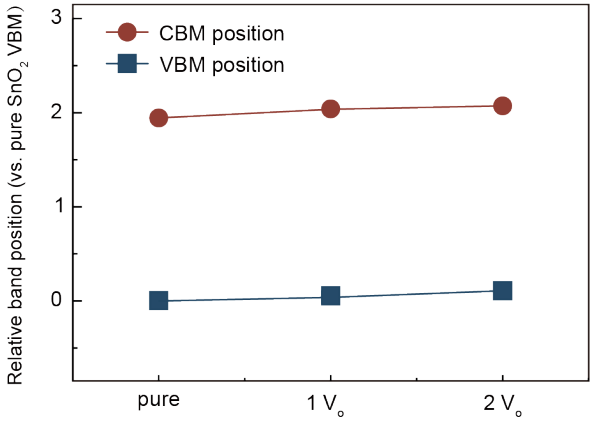

Supplementary Fig. 8 DFT calculation on SnO_2's band positions with varying V_o contents, showing an upward shift trend in both CBM and VBM position as the content of V_o increases.

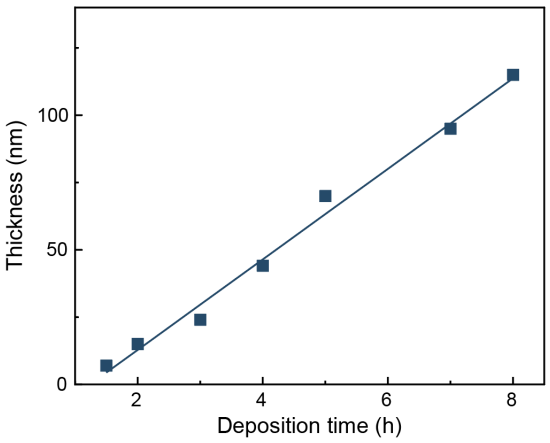

Supplementary Fig. 9 SnO_2 films thickness versus deposition time profile.

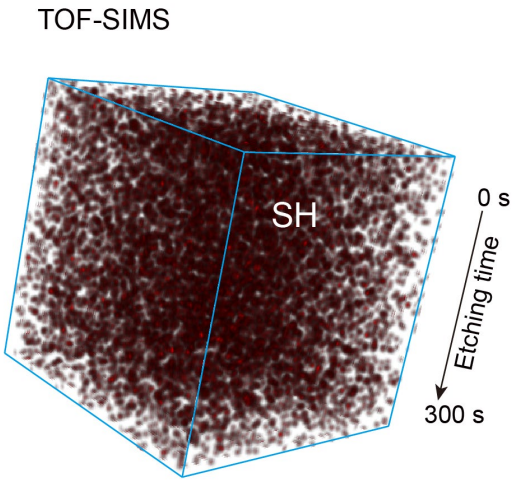

Supplementary Fig. 10 TOF-SIMS depth profile of -SH signal derived from TGA ligand in the control-SnO_2 ETL, showing a uniform distribution across the entire film thickness.

Supplementary Note 4 | Experimental and theoretical studies on electron property modulation.

1. Ligand interactions with SnO_2.

To clarify the chemical coordination between distinct head groups (COO^-, HPO_3^- and SO_3^-) and SnO_2, we performed Fourier-transform infrared (FTIR) spectroscopy. The spectra showed significant changes or disappearance of characteristic ligand peaks—C-OH at 1136 cm^{-1}, P-OH at 935 cm^{-1}, and SO_3H at 1030 cm^{-1} in MA-SnO_2, PA-SnO_2, SA-SnO_2, respectively. Additionally, peaks corresponding to C=O (1667 cm^{-1}), P-O (1034 cm^{-1}), and S=O (1300-1400 cm^{-1}) shifted to lower wavenumbers, indicating strong Sn-O interactions and electron transfer for each bidentate ligand.

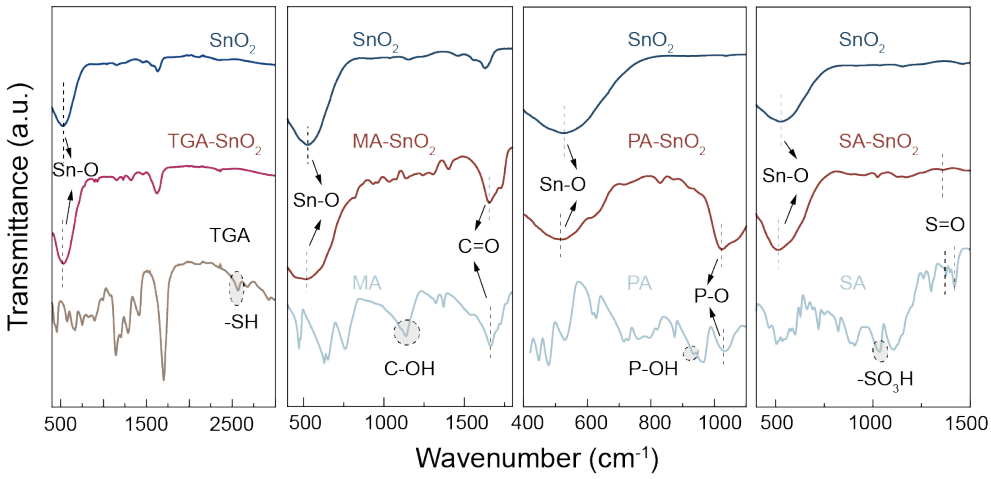

Supplementary Fig. 11 FTIR spectra of SnO_2 reference, bidentate ligands, and SnO_2 capped with TGA, MA, PA, SA ligands.

2. Ligand-regulated electronic property of SnO_2 ETL.

To modulate the oxygen vacancy concentration in SnO_2 ETL, we employed three ligands with distinct electron-withdrawing characteristics. DFT calculations showed that the minimum electrostatic potential (φ_{min}) of the ligand head-group anions followed the order MA < PA < SA (**Supplementary Fig. 12**). A lower φ_{min} corresponds to a more electron-rich functional group, indicating stronger electron-donating ability. This trend in electron donation was directly reflected in the ^{119}Sn-

NMR (**Supplementary Fig. 13**). As the electron-withdrawing strength of the ligand increases, the ^{119}Sn resonance peaks shift progressively toward higher chemical shift values, indicating a continuous decrease in electron density surrounding the Sn^{2+} centers. This spectroscopic evidence confirmed that the ligand's electronic properties are effectively transduced to the Sn^{2+} ions.

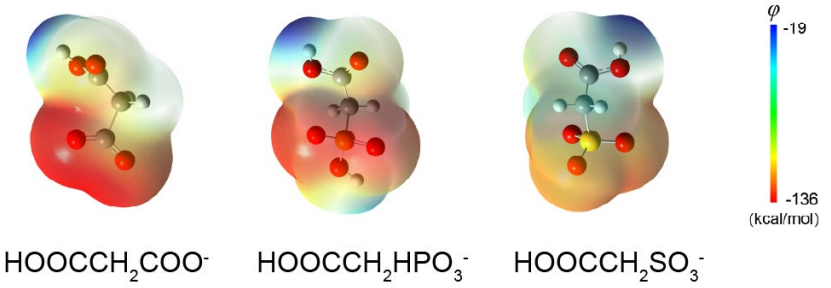

Supplementary Fig. 12 Structures and electrostatic potentials of different ligand anions.

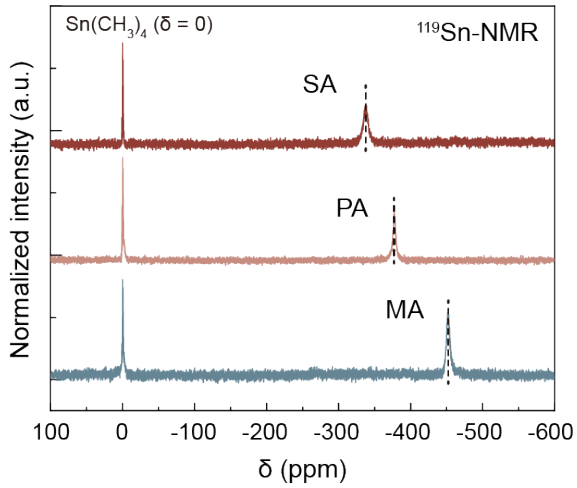

Supplementary Fig. 13 ^{119}Sn-NMR spectra with different ligand treatments.

The reduced electron density around Sn^{2+} in turn alters its redox behavior. Cyclic voltammetry measurements (**Supplementary Fig. 14a**) showed that ligands with stronger electron-withdrawing ability induce a more positive Sn^{2+}/Sn^{4+} oxidation potential, meaning that Sn^{2+} becomes more difficult to oxidize. Consequently, a higher fraction of Sn^{2+} remains in the as-deposited SnO_2 film, as corroborated by XPS analysis of Sn 3*d* XPS spectra (**Supplementary Fig. 15a**). The results showed a progressive increase in the Sn^{2+}/Sn^{4+} peak area ratio from 8.15% (TGA-SnO_2) to 10.13% (MA-SnO_2), 11.17% (PA-SnO_2), and 13.49% (SA-SnO_2), as well as V_o

contents (**Supplementary Fig. 15b**). Furthermore, in Sn *K*-edge XANES spectra (**Fig. 1e**), the absorption edges of MA-SnO_2, PA-SnO_2, and SA-SnO_2 progressively shifted toward that of the SnO reference, in contrast to TGA-SnO_2, indicating an increase in Sn^{2+} content.

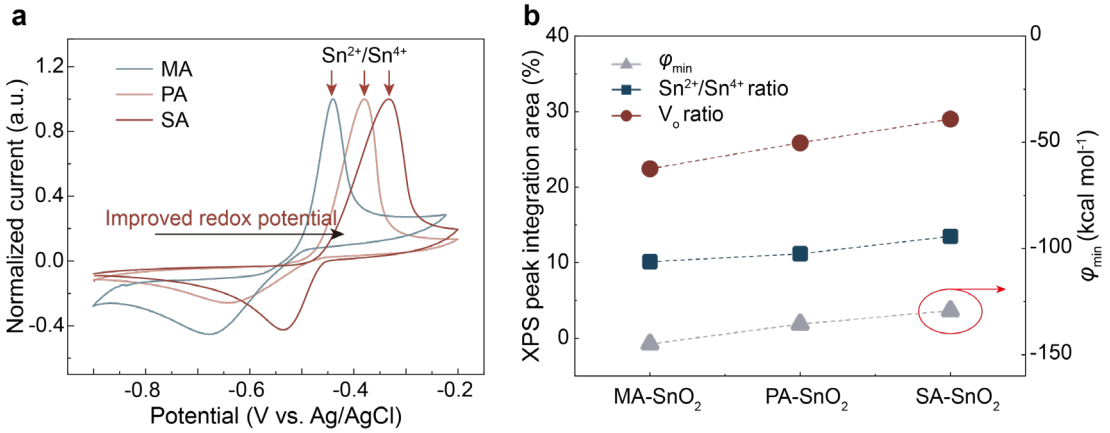

Supplementary Fig. 14 a, Sn^{2+}/Sn^{4+} redox potential under different ligands deposition measured by CV. **b**, The relationship between φ_{min} of bidentate ligands, Sn^{2+}/Sn^{4+}, and V_o area ratios extracted from XPS spectra of SnO_2 ETLs capped with different ligands.

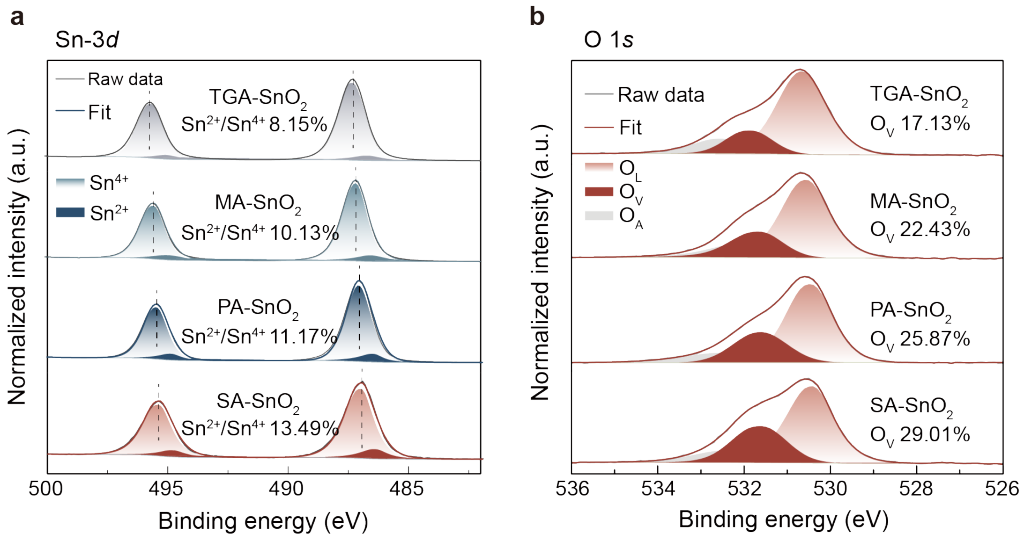

Supplementary Fig. 15 XPS spectra of Sn 3*d* (**a**) and O 1*s* (**b**) for TGA-SnO_2, MA-SnO_2, PA-SnO_2, SA-SnO_2, respectively.

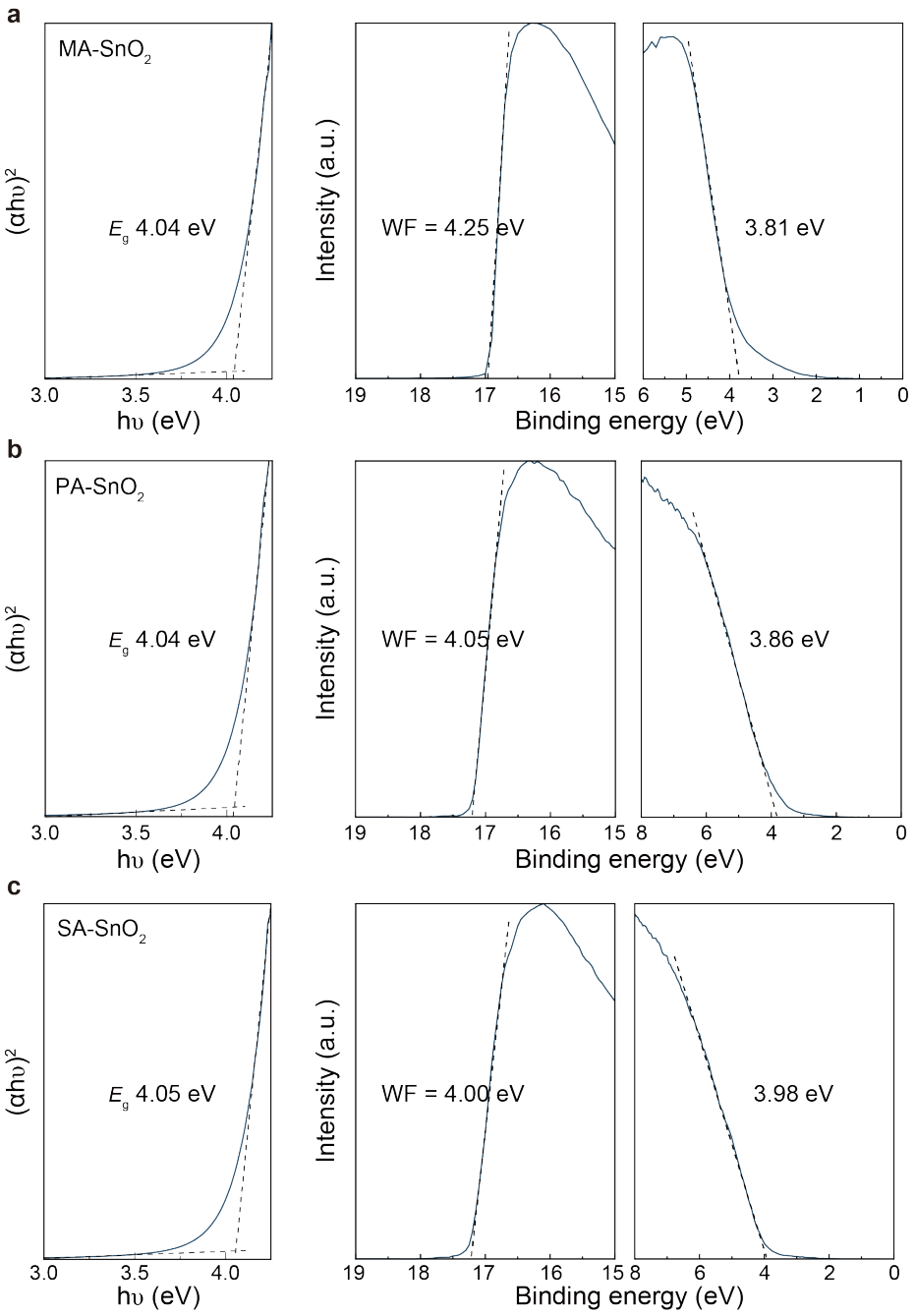

Supplementary Fig. 16 UV-vis absorption (left) and secondary electron cut-off region and valence photoemission spectra (right) of UPS spectra for MA-SnO_2 (**a**), PA-SnO_2 (**b**), SA-SnO_2 (**c**), respectively.

The band structure and doping density of TGA-SnO_2, MA-SnO_2, PA-SnO_2, SA-SnO_2 ETLs, as determined by Hall effect measurements, were summarized in **Supplementary Table 1**.

Supplementary Table 1. Summary of the band structure and carrier density measured by Hall effect for SnO_2 ETLs with different ligands.

Sample	E_F (eV)	CBM (eV)	VBM (eV)	Hall effect Carrier density n (cm^{-3})
TGA-SnO_2	-4.39	-4.13	-8.16	3.94×10^{15}
MA-SnO_2	-4.25	-4.02	-8.06	1.02×10^{16}
PA-SnO_2	-4.05	-3.87	-7.91	9.25×10^{16}
SA-SnO_2	-4.00	-3.93	-7.98	9.94×10^{17}

Furthermore, to assess whether bidentate ligands with higher φ_{min} are compatible with high-performance device fabrication, we performed DFT calculations on 12 candidate ligands, systematically varying the head group chemistry and introducing electron withdrawing substituents on the aromatic backbone. As shown in **Supplementary Fig. 17**, the calculated φ_{min} values range from -142.62 to -119.52 kcal/mol. Notably, several molecules, including compounds (4) through (12), exhibited φ_{min} values higher than that of SA (-129.28 kcal/mol). To experimentally evaluate the impact of such higher φ_{min} ligands on resulting SnO_2 properties, we herein selected three commercially available candidate ligands: *o*-SBA (-127.38 kcal/mol), *p*-SBA (-124.16 kcal/mol), and 4F-SBA (-119.52 kcal/mol), highlighted in the red box.

Given that higher φ_{min} leads to a higher oxygen vacancy concentration and an upward-shifted CBM, we anticipated that such ligands might further optimize the SnO_2/perovskite interface. However, when these SnO_2 ETLs were integrated into devices using the same perovskite absorber, no improvement in efficiency was observed; in some cases, performance deteriorated relative to the SA-based control (**Supplementary Fig. 18**). This outcome was attributed to the critical role of band

alignment. While a higher φ_{min} increases the SnO_2 CBM, excessively large CBM offset can introduce an undesirable energetic barrier at the electron extraction interface, impeding charge transfer and increasing recombination. In other words, φ_{min} is not a parameter to be maximized in isolation; rather, its optimal value depends on the specific perovskite composition and the desired alignment of energy levels.

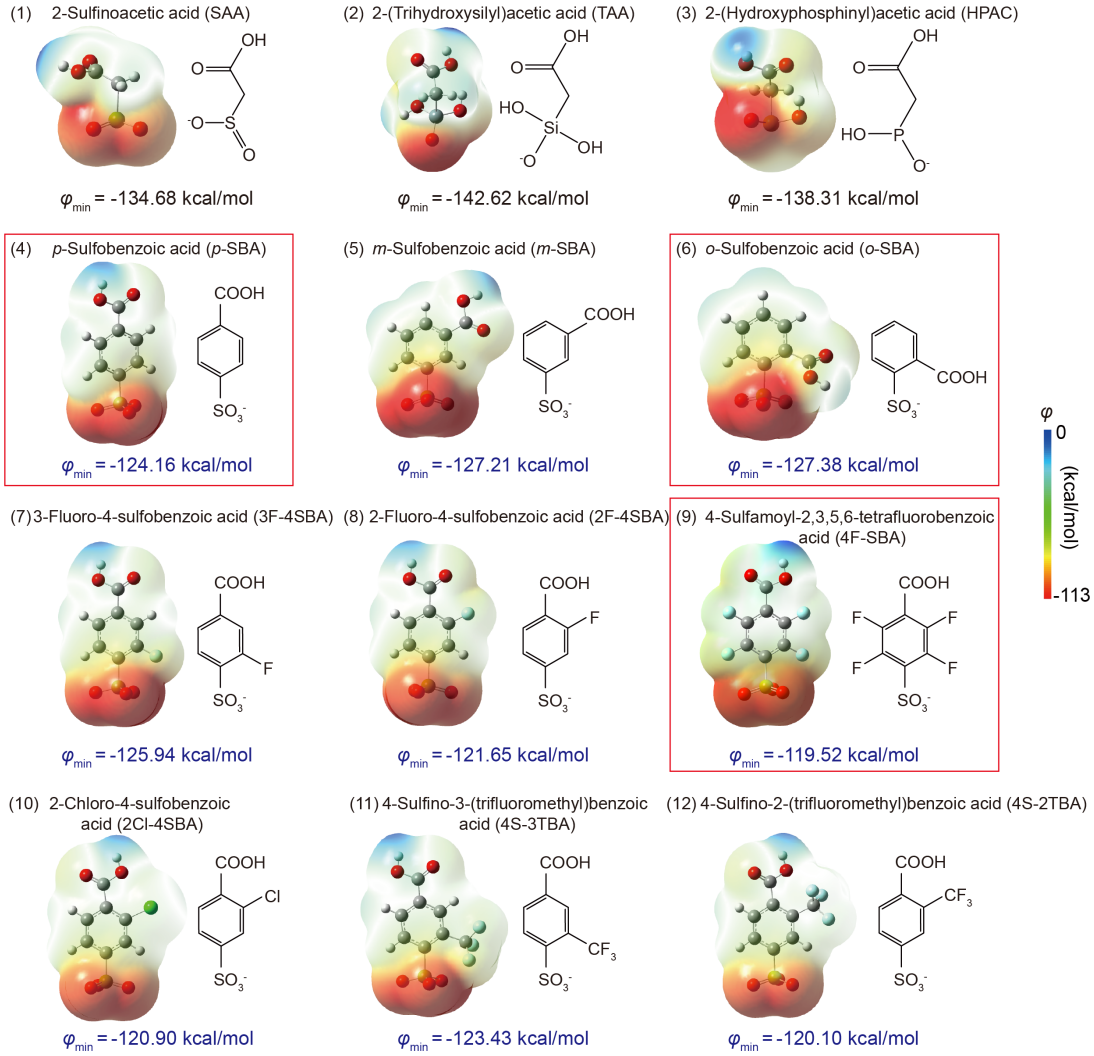

Supplementary Fig. 17 Structures and electrostatic potentials of different bidentate ligand anions.

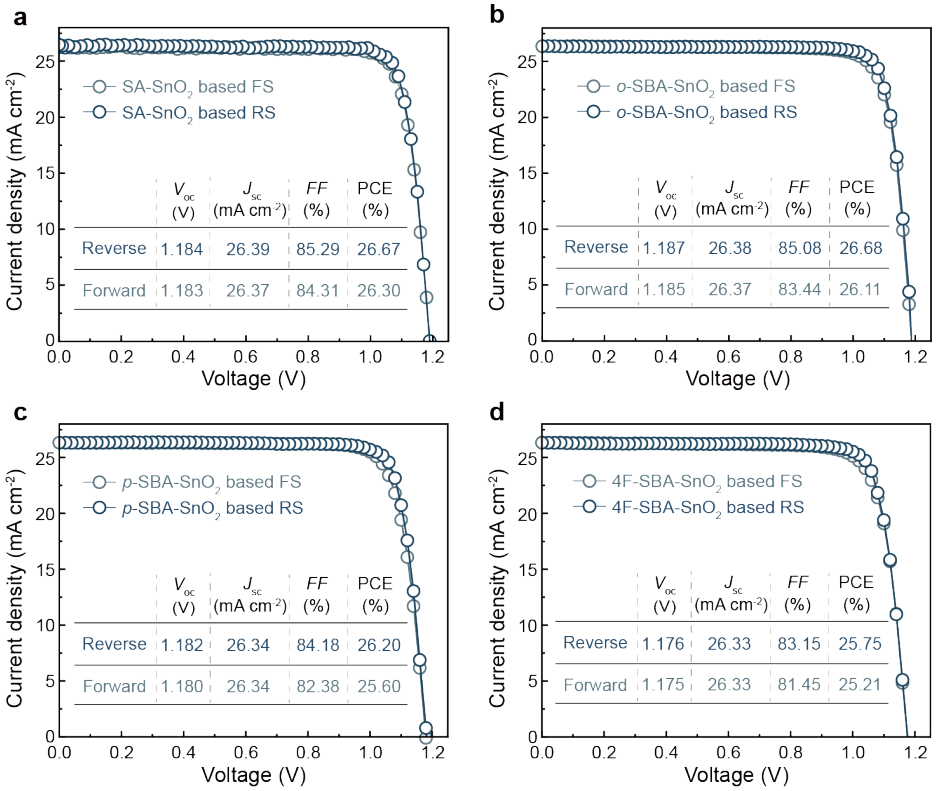

Supplementary Fig. 18 *J-V* curves for SA-SnO_2 (**a**), *o*-SBA-SnO_2 (**b**), *p*-SBA-SnO_2 (**c**), 4F-SBA-SnO_2 (**d**) based devices, respectively.

Supplementary Note 5 | SCAPS-1D simulations for diverse ligand-capped SnO_2 stacks.

To elucidate the impact of diverse ligand-capped SnO_2 stacking configurations on device performance, we performed SCAPS-1D simulations on three representative architectures: a homogeneous ligand-capped SnO_2 single ETL, a discrete bilayer and a continuously graded-doped structure. As shown in **Supplementary Figs. 19a**, **b**, despite under identical interface defect density and band alignment between pure PA-capped SnO_2 and graded SnO_2, the continuously graded-doped SnO_2 ETL exhibited a pronounced performance enhancement (~2.1% efficiency gain). Moreover, devices with a continuously graded-doped ETL consistently outperformed the discrete bilayer, delivering an ~1.94% efficiency gain (**Supplementary Figs. 19a**, **c**).

Collectively, these results indicated that the continuously graded-doped SA-SnO_2 (n^+)/PA-SnO_2 (n) ETL enabled optimized band alignment and a strengthened built-in electric field, serving as the dominant device stack responsible for achieving high-efficiency performance.

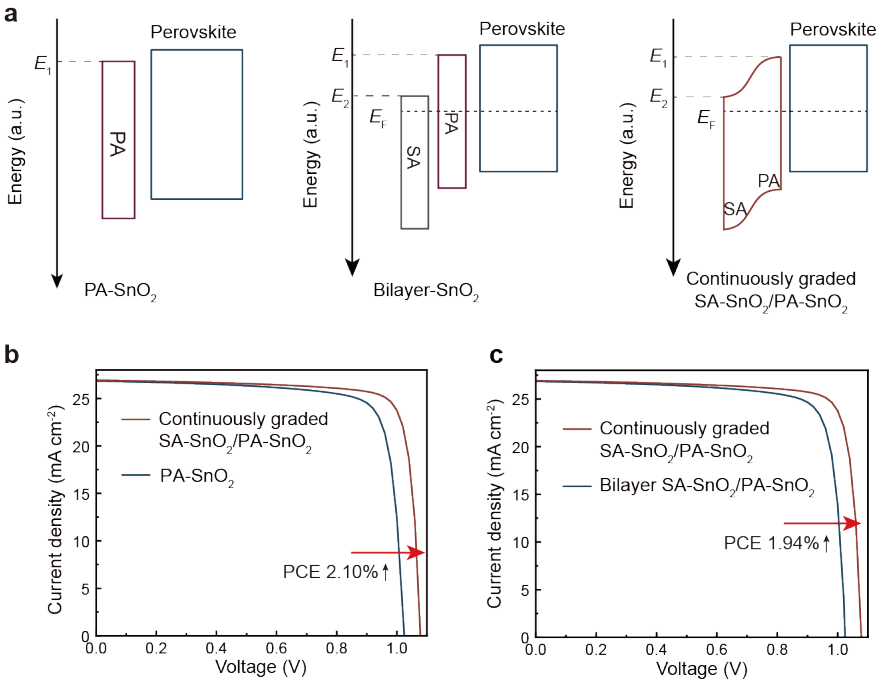

Supplementary Fig. 19 a, Schematics of devices stacks based on PA-SnO_2 or bilayer SnO_2 or continuously graded SnO_2 ETL, respectively. **b**, **c** Simulated *J-V* curves based on PA-SnO_2 or bilayer SnO_2 compared with continuously graded ETL.

Supplementary Table 2. Material parameters used for simulation in SCAPS-1D[9].

Parameter	Material		
	ETL	Perovskite	HTL
Electron Affinity (eV)	Various	3.83	2.20
Dielectric permittivity (relative)	25	24.1	3
Conduction band effective density of states (cm^{-3})	4.1×10^{18}	7.9×10^{17}	2.2×10^{18}
Valence band effective density of states (cm^{-3})	1×10^{18}	1×10^{18}	2.2×10^{18}
Electron mobility ($cm^2\ V^{-1}\ s^{-1}$)	6.8×10^{-4}	2.2×10^{1}	1×10^{-3}
Hole mobility ($cm^2\ V^{-1}\ s^{-1}$)	1×10^{2}	2.2×10^{1}	1×10^{-3}
Shallow uniform donor density, ND (cm^{-3})	Various	0	0
Shallow uniform acceptor density, NA (cm^{-3})	0	1×10^{15}	1.3×10^{18}

Supplementary Note 6 | Ligands competitive binding dynamics.

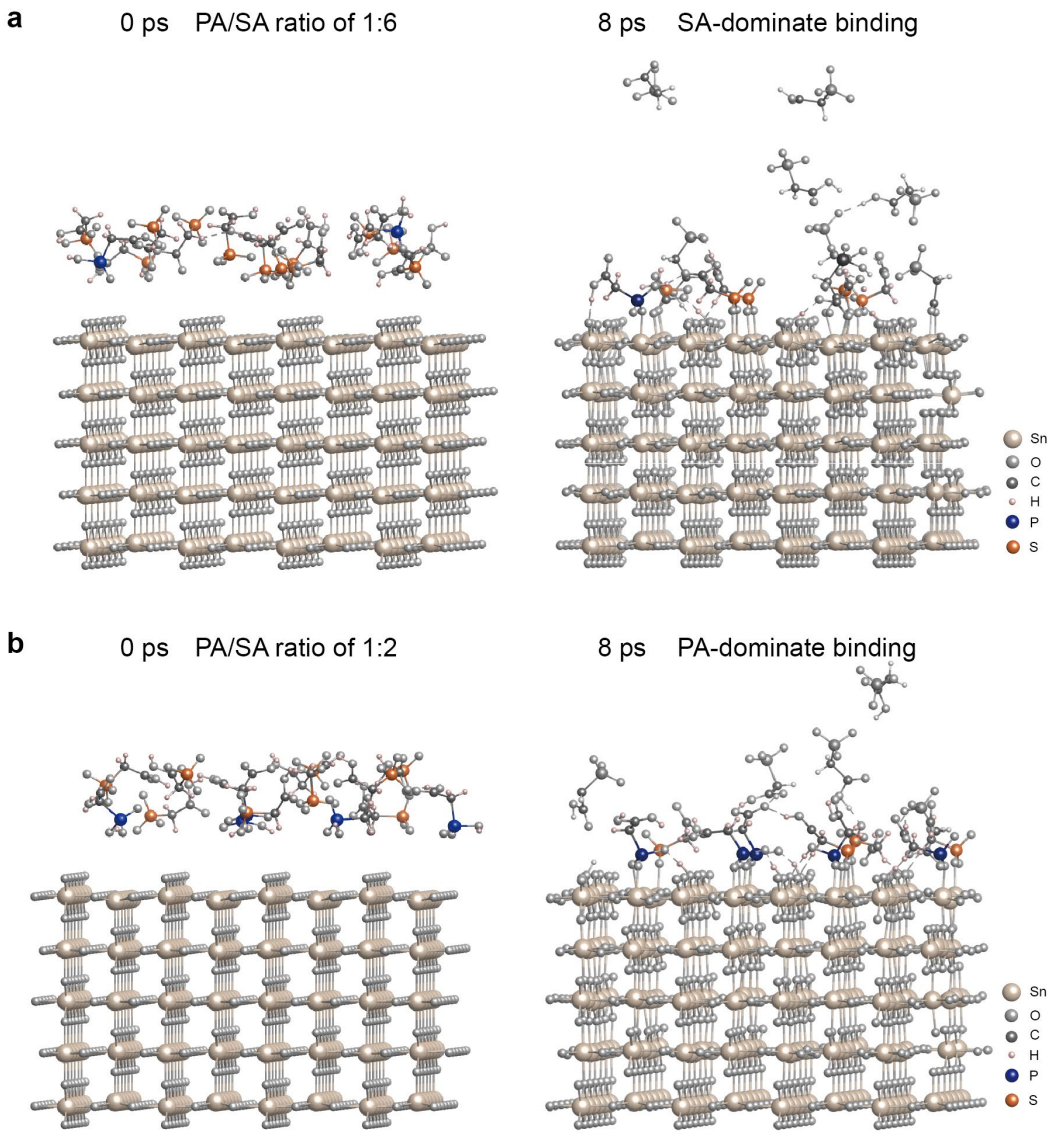

Supplementary Fig. 20 AIMD simulations of ligands binding under different PA/SA ratios. **a**, Initial (left) and AIMD-relaxed (right) configurations for a PA/SA ratio of 1:6. **b**, Initial (left) and AIMD-relaxed (right) configurations for a PA/SA ratio of 1:2.

Real-time monitoring of DMPA hydrolysis: The hydrolysis kinetics of DMPA were monitored directly during the CBD process using ^{31}P-NMR spectroscopy, which provides well-resolved spectral signatures for DMPA and its hydrolysis product, phosphonic acid (PA), with H_3PO_4 as an internal standard (**Supplementary Fig. 21a**). Spectra were acquired at 1 h intervals throughout the deposition. By integrating the peak areas corresponding to PA and DMPA, we quantified the PA conversion rate (x) as a function of time, which increased from 2.6% at 1 h to 9.4% at 5 h (**Supplementary Fig. 21b**). This partial hydrolysis is not a limitation but rather a deliberate feature of our strategy: DMPA serves as a slow-release precursor that continuously supplies PA ligands over the deposition period, enabling the formation of a graded ligand distribution without requiring full conversion.

Fitting the conversion data to a first-order kinetic model yielded the rate equation: $[A] = [A]_0 \exp(-4.845 \times 10^{-6} t)$ and $\ln(1-x) = -4.845 \times 10^{-6} t$, describing the conversion from DMPA to PA ($[A]_0$ and $[A]$ denote the initial and time-dependent concentrations of DMPA, respectively). This model quantitatively described the conversion from DMPA to PA under our deposition conditions.

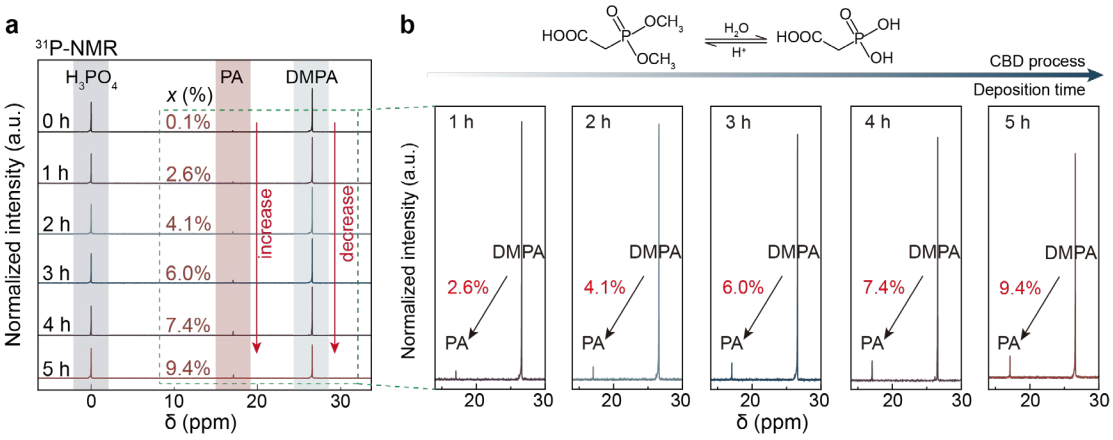

Supplementary Fig. 21 a, ^{31}P-NMR spectra of DMPA into PA at different deposition times during CBD process, with H_3PO_4 used as the internal standard. **b**, Enlarged ^{31}P-NMR spectra of DMPA to PA during CBD process.

The process followed first-order reaction behavior, which was accurately described by equation 6-7.

$$r = -\frac{d[A]}{dt} = k[A] \qquad [A] = [A]_0 e^{-kt} \qquad 6$$

$$x = \frac{[A]_0 - [A]}{[A]_0} \qquad \ln(1-x) = -kt \qquad 7$$

To experimentally validate this kinetic model, we monitored the consumption of tin ions using inductively coupled plasma spectroscopy (ICP)[10]. We found that the tin consumption rate in SA-DMPA system gradually evolved from being comparable to that of pure SA to approaching that of pure PA, in excellent agreement with the theoretical predictions.

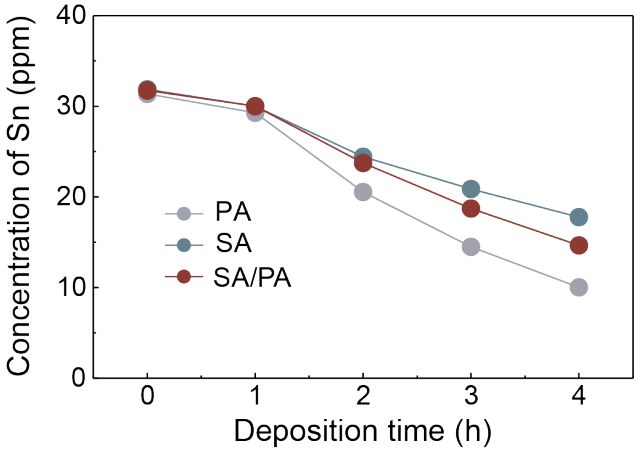

Supplementary Fig. 22 Time-dependent evolution of Sn concentration in the CBD solution, quantified by ICP measurements.

To directly assess whether DMPA itself incorporates into the film, we fabricated SnO_2 ETLs using DMPA as the sole additive. Cross-sectional SEM images first confirmed that DMPA enabled conformal coverage comparable to that achieved with PA ligands (**Supplementary Fig. 23**).

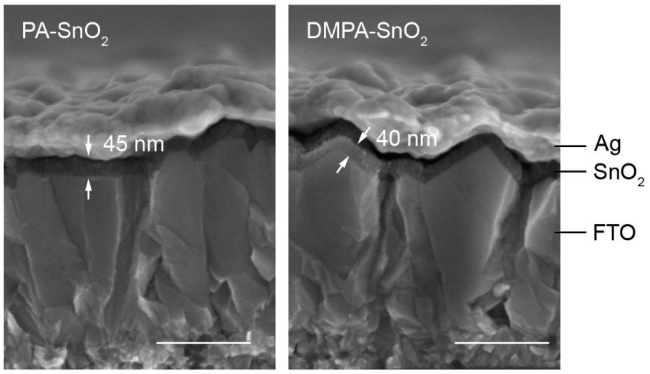

Supplementary Fig. 23 Cross-section SEM images of PA-SnO_2 and DMPA-SnO_2.

To further determine the chemical composition, TOF-SIMS measurements were performed on the as-deposited film prior to annealing (**Supplementary Fig. 24**). Across the entire film depth, no ester-related fragments characteristic of DMPA were detected. Instead, PO_2^- signals, originating from the hydrolyzed PA ligand, were uniformly distributed throughout the SnO_2 layer. These results unequivocally demonstrated that the deposited film consists of PA-capped SnO_2, not DMPA-capped SnO_2.

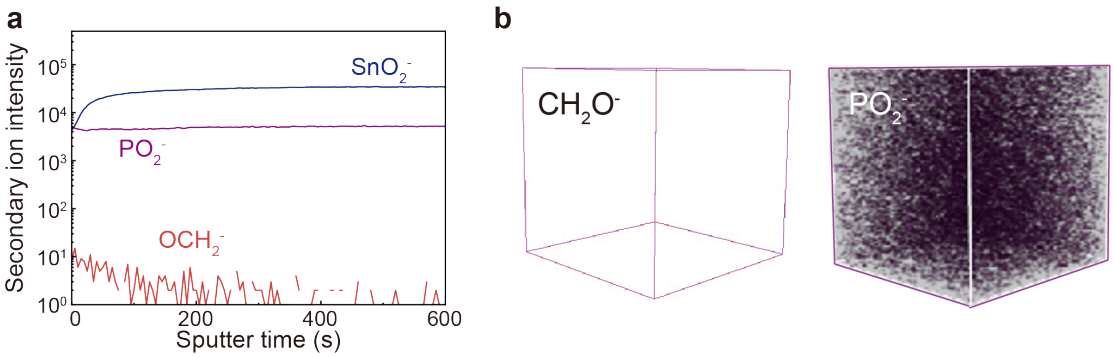

Supplementary Fig. 24 TOF-SIMS depth profiles (**a**) and corresponding 3D mapping (**b**) of a SnO_2 film deposited using DMPA additive without annealing.

This conclusion was further supported by DFT calculations and growth-mechanism analysis. Binding-energy calculations revealed that the ester group "-$PO(OCH_3)_2$" of DMPA exhibited substantially weaker binding to Sn^{2+} than the sulfonic acid head group of SA (**Supplementary Fig. 25**). Moreover, even if the -COOH group of DMPA were to bind to Sn, the ester tail group lacks the ability to generate a negatively charged nanoparticle surface, a prerequisite for electrostatic adsorption onto the FTO substrate. Consequently, the formation of a DMPA-capped SnO_2 layer is thermodynamically and kinetically unfavorable under our deposition conditions.

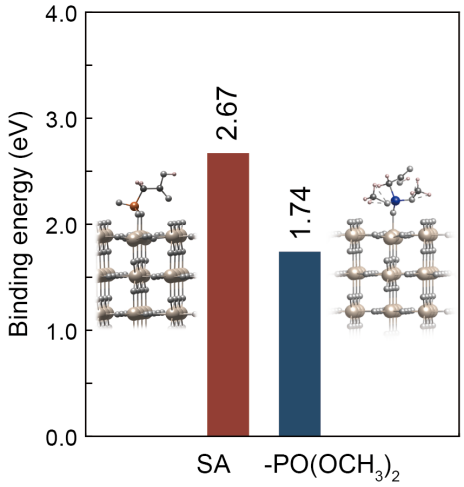

Supplementary Fig. 25 Calculated binding energy of SA and -$PO(OCH_3)_2$ group from DMPA ligands on SnO_2 surfaces.

Supplementary Note 7 | Characterization of continuously graded-doped SnO_2 ETL.

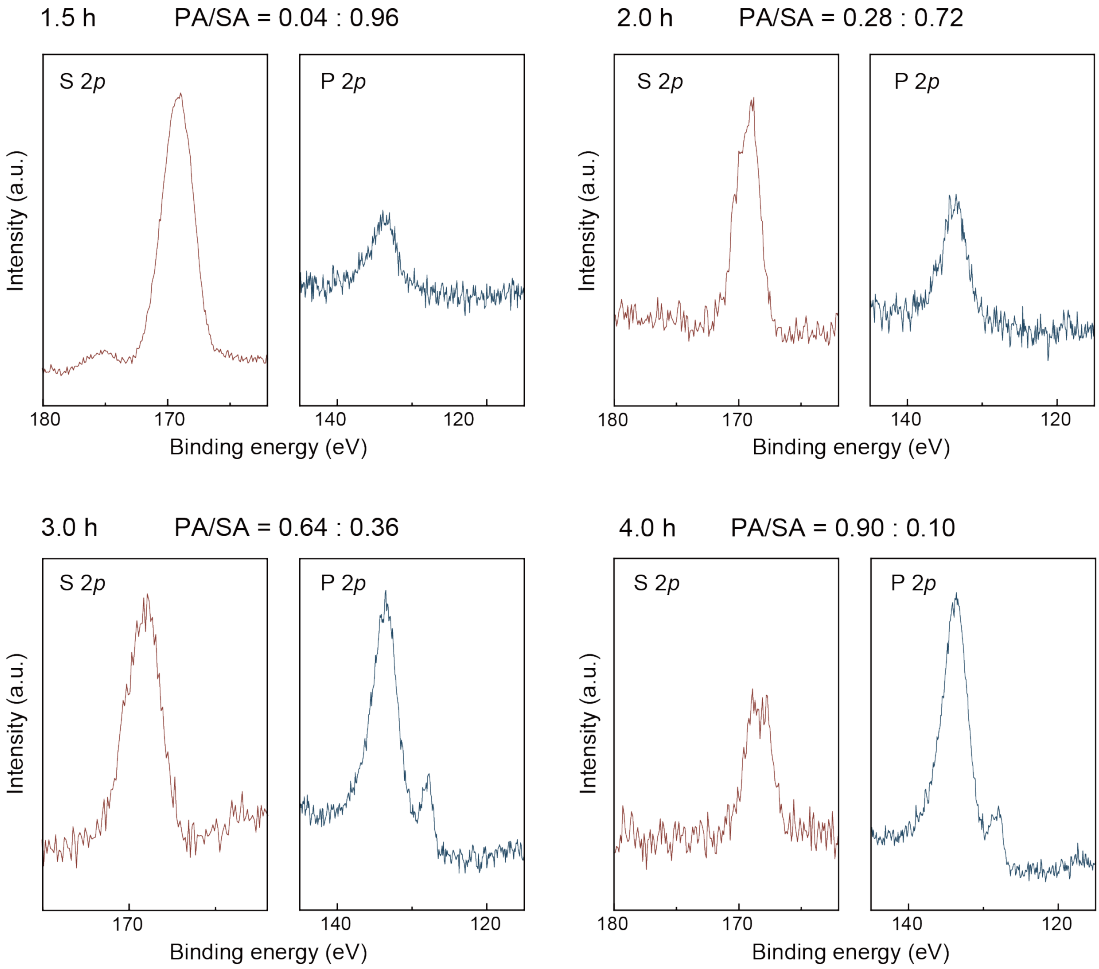

Supplementary Fig. 26 XPS spectra of P 2*p* and S 2*p* signal at varying deposition time.

Supplementary Table 3. Quantitative analysis of the atomic ratio between PA and SA molecules based on XPS spectra.

Deposition time (h)	1.5 h	2.0 h	3.0 h	4.0 h
Peak area of P 2*p*	2,759.17	2,311.77	2,229.50	27,703.65
Peak area of S 2*p*	82,667.55	8,077.77	1,697.82	4,312.01
PA/SA atomic ratio	0.04:0.96	0.28:0.72	0.64:0.36	0.90:0.10

Supplementary Note 8 | Conformal and graded SnO_2 deposition on textured substrates with varying roughness.

As described in the manuscript, textured FTO substrates effectively reduces front-surface reflection and increases the optical path length within the perovskite layer, representing a well-established strategy for enhancing photon harvesting. To evaluate the compatibility of the CBD process with substrates of varying RMS values, we selected three substrates with distinctly different surface morphologies, as characterized by AFM measurements (**Supplementary Fig. 27**): a low-texture FTO substrate (FTO-1, RMS = 12 nm, pyramids height ~60 nm), a moderately textured FTO substrate (FTO-2, RMS = 43.9 nm, pyramids height ~200 nm, used in this work), and a highly textured Si substrate (Si, RMS = 400 nm, pyramids height ~2-3 μm as confirmed by cross-sectional HAADF-STEM). SnO_2 ETLs were then deposited onto each of these substrates using the same CBD process.

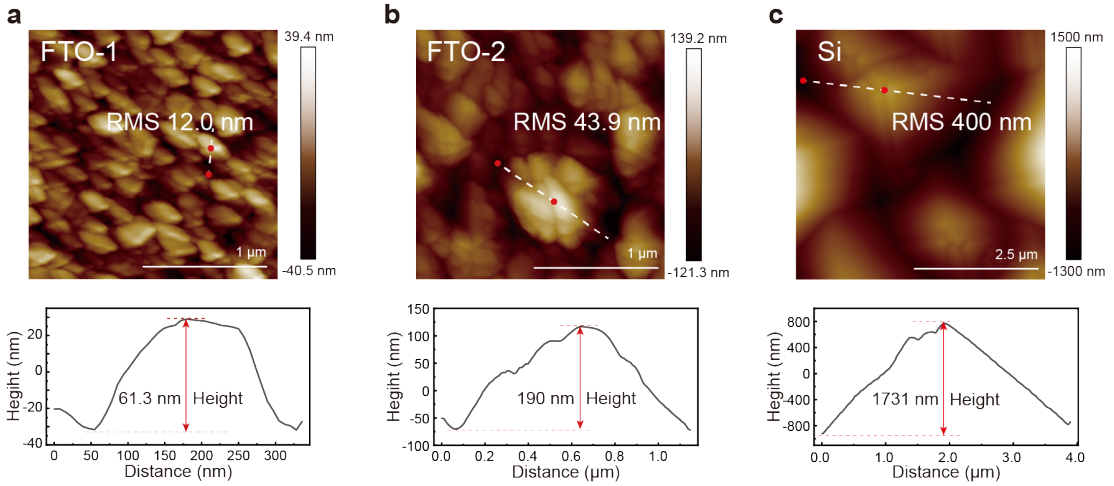

Supplementary Fig. 27 AFM images and the height distribution profile along with the white dashed line region for FTO-1 (**a**), FTO-2 (**b**), Si (**c**) substrates, respectively.

To assess whether conformal coverage can be achieved across substrates with markedly different surface textures, we performed cross-sectional HAADF-STEM measurements on the three representative samples. As shown in **Supplementary Figs. 28-29**, uniform and conformal SnO_2 ETLs were successfully deposited on all substrates, ranging from nanoscale FTO pyramids (~50-200 nm) to micro-scale Si pyramids (~3 μm). These results confirmed the excellent conformality and broad

substrate adaptability of the CBD process.

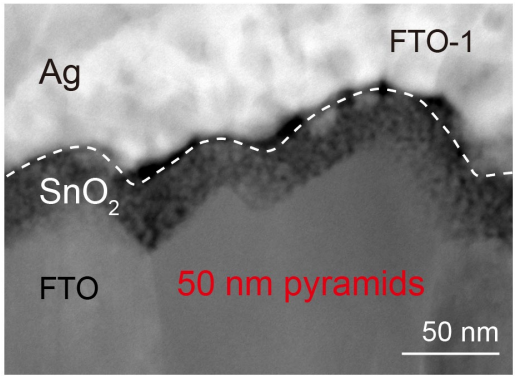

Supplementary Fig. 28 Cross-sectional HAADF-STEM images of CBD SnO_2 deposited on FTO-1 substrates.

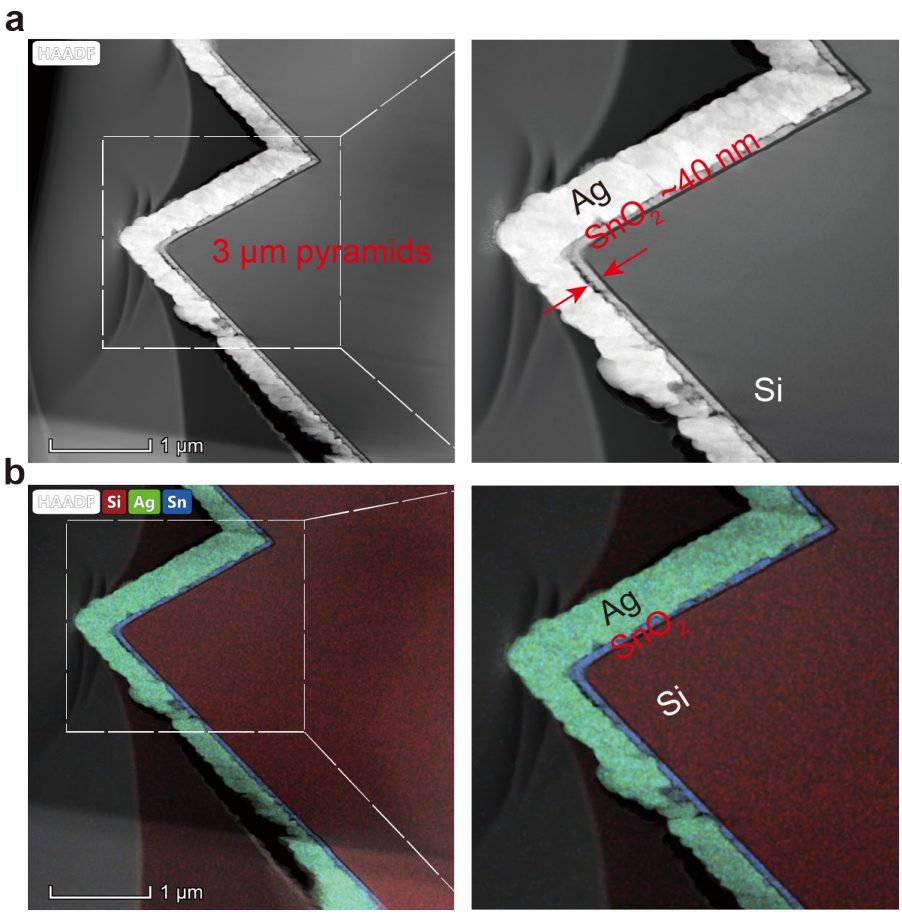

Supplementary Fig. 29 Cross-sectional HAADF-STEM images (**a**) and EDS maps (**b**) of CBD SnO_2 deposited on Si substrate with 3 μm pyramids, the right images were enlarged pictures.

To quantify the optical contribution, we performed 3D FDTD simulations combined with APSYS software. As shown in **Supplementary Fig. 30**, the presence

of textured substrates indeed enhanced the corresponding photocurrent density (J_{sc}) of the devices. Relative to a conventional substrate with 100 nm pyramid height, the 200 nm texture used in our work yields an additional ~0.4 mA cm^{-2} in J_{sc}, unambiguously demonstrating the critical role of substrate texturing in light management. However, the simulations further revealed that when pyramid heights approach the microscale, comparable to those used in silicon photovoltaics, no significant photocurrent gain was observed in PSCs with absorber thicknesses on the order of hundreds of nanometers. These results collectively demonstrated that nanoscale texturing is more suitable for single-junction perovskite solar cells, offering an optimal balance between optical performance and compatibility with thin-film device constraints.

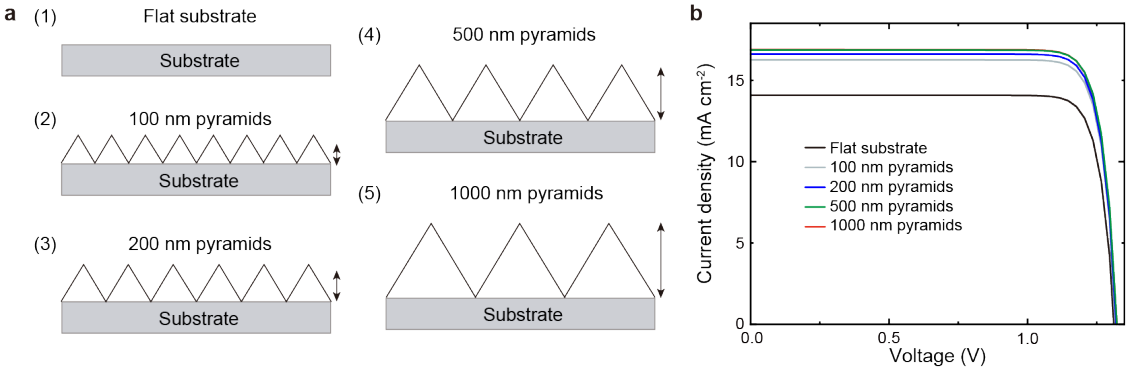

Supplementary Fig. 30 a, Schematic illustrations of FTO substrates with different pyramids heights. **b**, Simulated *J-V* curves of devices based on FTO substrates with varying pyramid heights.

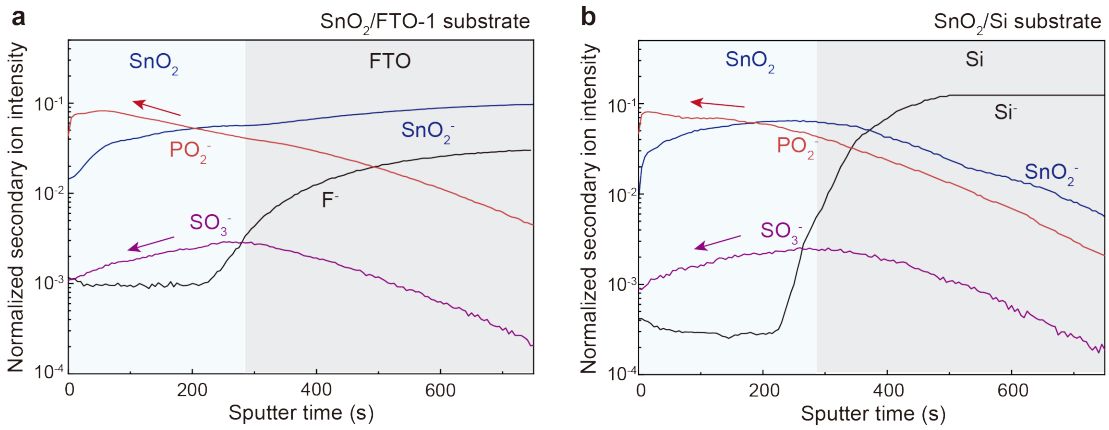

Supplementary Fig. 31 TOF-SIMS depth profiles of PO_2^- from PA and SO_3^- from SA for SnO_2 film deposited on FTO substrate with ~60 nm pyramids (**a**) and Si substrate with ~3 μm pyramids (**b**).

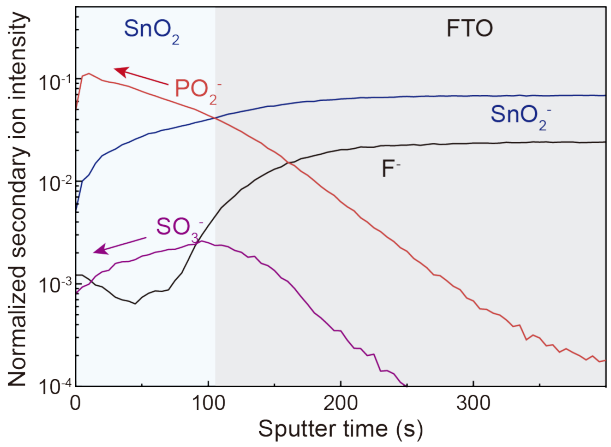

Supplementary Fig. 32 TOF-SIMS depth profiles of PO_2^- from PA and SO_3^- from SA for SnO_2 ETL with 1 h deposition.

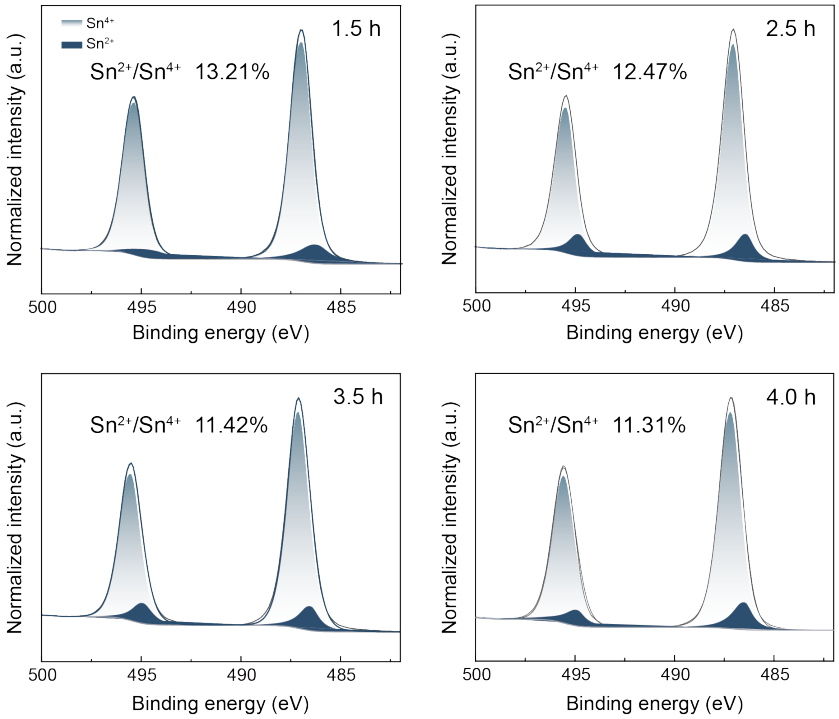

Supplementary Fig. 33 Sn 3*d* XPS spectra of LCB-derived SnO_2 film at varying deposition time.

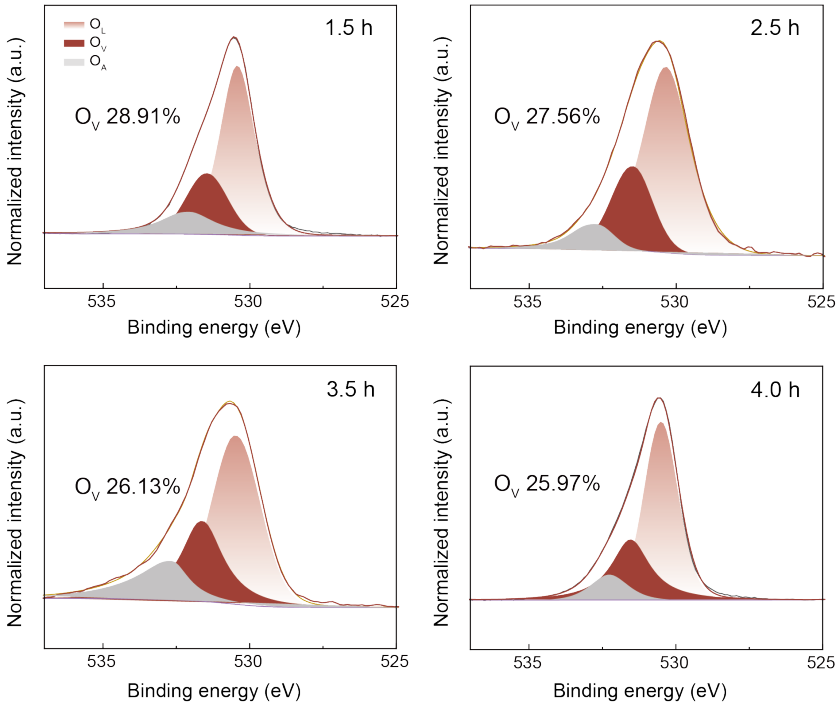

Supplementary Fig. 34 O 1*s* XPS spectra of LCB-derived SnO_2 film at varying deposition time.

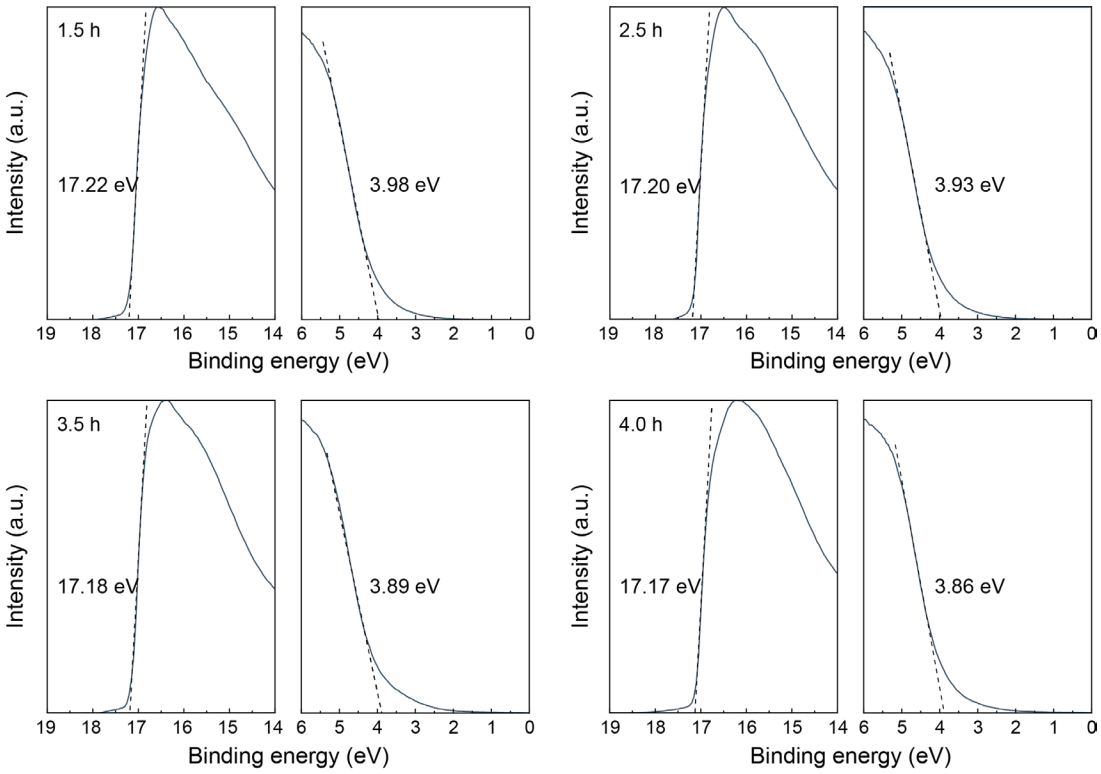

Supplementary Fig. 35 UPS spectra of LCB-derived SnO_2 film at varying deposition times.

According to Fermi-Dirac statistical distribution, it is revealed that an increase in the energy difference between E_F and E_{CB} (ΔE_F - E_{CB}) results in a higher carrier concentration in SnO_2, thereby enhancing n-doping characteristics[11].

$$E_{CB} = E_F - \frac{k_B T}{e} \ln\left(\frac{N_C}{N_D}\right) \quad 8$$

where N_c is the effective density of conduction band states, N_D is the charge carrier concentration, E_{CB} is the conduction band potential, E_F is the fermi level potential.

Supplementary Note 9 | Buried interface property based on continuously graded-doped SnO_2 ETL.

To assess whether the surface ligands perturb the initial nucleation and grain growth of the overlying perovskite, we deposited perovskite films on three types of SnO_2 substrates: TGA-capped SnO_2 (control), continuously graded SA-SnO_2/PA-SnO_2 (target structure), and ligand-free SnO_2 fabricated by atomic layer deposition (ALD-SnO_2).

As shown in **Supplementary Fig. 36**, the perovskite precursor solution exhibited comparable contact angles on all three substrates, indicating similar nucleation behavior. This was attributed to the comparable surface polarity across substrates: both TGA-SnO_2 and graded-SnO_2 were terminated with -COOH groups, while ALD-SnO_2 becomes hydroxyl-terminated (-OH) upon air exposure[12], affording similar wettability.

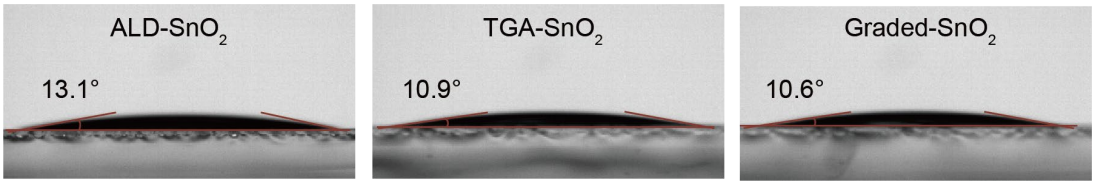

Supplementary Fig. 36 Contact angles of perovskite solution upon different SnO_2 substrates.

We then monitored the perovskite crystallization process during spin coating using *in-situ* time-resolved PL measurements (**Supplementary Fig. 37**). In all three cases, an intense PL peak centered at ~770 nm, assigned to the perovskite intermediate phase, emerged immediately after antisolvent dripping. The temporal evolution of the peak position followed nearly identical trajectories across substrates, with no observable shift, indicating similar crystallization kinetics and phase-conversion pathways. Furthermore, the full width at half maximum (FWHM) of the PL spectra remained comparable, suggesting that the crystallization quality was unaffected by the underlying substrate.

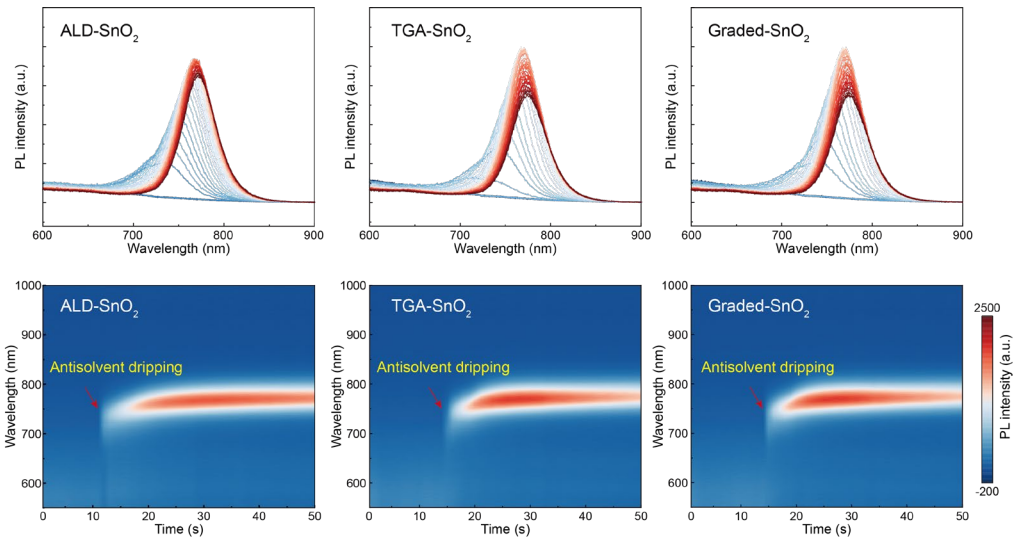

Supplementary Fig. 37 In-situ time-resolved PL spectra for perovskite crystallization during deposition on different SnO_2 ETL substrates at spin-coating stage.

Top-view SEM imaging revealed that the perovskite films grown on different substrates exhibited nearly identical grain size and morphology (**Supplementary Fig. 38**). Collectively, these results confirmed that the residual ligands in the continuously graded SnO_2 do not measurably influence the nucleation, crystallization kinetics, or final grain structure of the overlying perovskite layer.

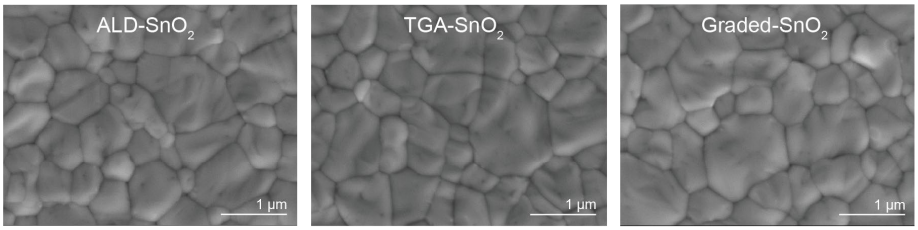

Supplementary Fig. 38 SEM images from top view of perovskite layers deposited on different SnO_2 ETL substrates.

To directly probe the interfacial composition, we performed cross-sectional TEM and XPS depth profiling.

As shown in **Supplementary Fig. 39**, a sharp, well-defined interface was observed between the SnO_2 and perovskite layers.

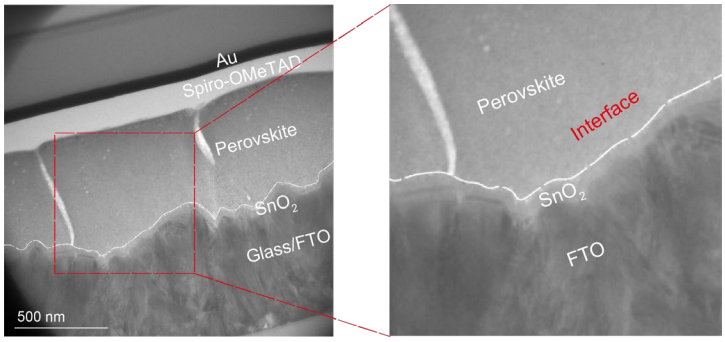

Supplementary Fig. 39 TEM images of n-i-p perovskite solar cell.

To further resolve the interfacial chemical states, we conducted XPS measurements with sequential argon cluster ion beam (GCIB) sputtering (**Supplementary Fig. 40a**). The emergence of the Pb 4*f* signal concurrent with a weak Sn 3*d* signal was used to identify the buried interfacial region. As shown in **Supplementary Figs. 40b-c**, the Pb *4f* spectra acquired from the buried interface exhibited no additional shoulder peaks, no peak shifts, and no broadening compared to those from the bulk perovskite. This indicated that Pb^{2+} remained in its native coordination environment without detectable formation of Pb-sulfonate, Pb-phosphonate, or other insulating lead-based compounds.

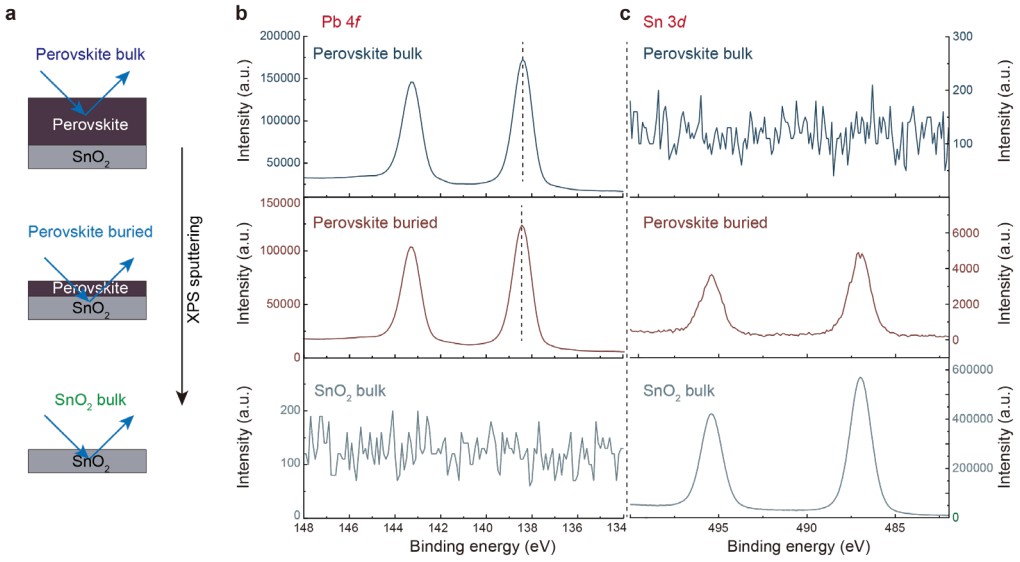

Supplementary Fig. 40 a, Schematic illustration of XPS sputtering and signal detection. XPS spectra of Pb 4*f* (**b**) and Sn 3*d* (**c**) corresponding to the perovskite bulk, buried interface, and SnO_2 bulk region, respectively.

Supplementary Note 10 | Improvement of device performance for continuously graded-doped SnO_2 ETL.

To experimentally validate the advantages of the continuously graded-doped SnO_2 ETL in electron extraction and device performance, we constructed a series of well-controlled comparative systems, including discrete bilayer structure, homogeneously ligand-capped SnO_2, and alternative gradient fabrication approaches.

1. Firstly, compared with the control-SnO_2 ETL, the continuously graded-doped SnO_2 ETL exhibited markedly enhanced electron-extraction efficiency and interfacial extraction kinetics (**Supplementary Table 4**). This improvement substantially reduced both charge-transfer and transport resistances, as confirmed by electrochemical impedance spectroscopy (**Supplementary Fig. 41a**), leading to a pronounced increase in device efficiency from 26.01% to 27.64% (**Extended Data Fig. 2**). Notably, SCLC measurements of electron-only devices based on the graded-doped SnO_2 showed a defect density comparable to that of TGA-SnO_2 (**Supplementary Fig. 41b**). This result further confirmed that the non-radiative recombination loss at the buried interface primarily originated from the suppressed electron extraction capability, rather than defect passivation.

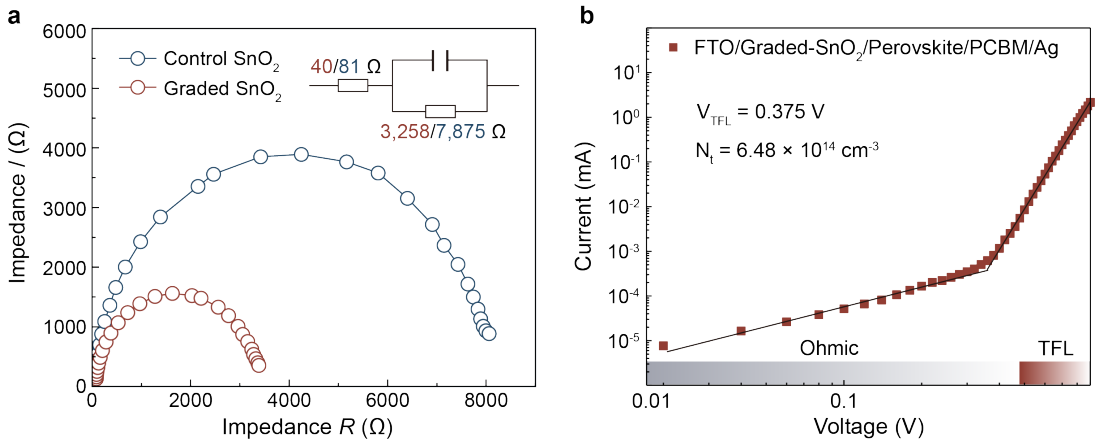

Supplementary Fig. 41 a, EIS spectroscopy of the devices based on control-SnO_2 and continuously graded-doped SnO_2. **b**, SCLC curves for the electron-only device based on continuously graded-doped SnO_2, respectively.

Supplementary Table 4. TRPL fitting parameters for diverse stacks.

Sample	τ_{ave} (ns)	k_{ET} (s^{-1})	η (%)
Perovskite	3,090.1	-	-
Control-SnO_2/perovskite	86.7	1.15×10^7	97.14
PA-SnO_2/perovskite	39.96	2.5×10^7	98.72
Bilayer-SnO_2/perovskite	27.1	3.69×10^7	99.13
Continuously graded-SnO_2/perovskite	23.9	4.18×10^7	99.19
Perovskite/HTL	23.2	4.27×10^7	99.21

2. Second, to decouple the effect of graded-doping from those of interface passivation, we designed two control systems that isolate the influence of the graded distribution while preserving the ligand chemistry at the interface or within the bulk (**Supplementary Fig. 42**).

Pure PA-capped SnO_2 (no graded doping, but identical interfacial chemistry): This ETL shares the same PA ligand termination at the perovskite interface as the graded ETL, ensuring identical chemical passivation at the contact, but lacks the graded doping profile (**Supplementary Fig. 42b**).

Mixed PA/SA-capped SnO_2 (no graded doping, but identical bulk ligand composition): By introducing PA and SA ligands at a 1:4 molar ratio during synthesis, we obtained SnO_2 nanoparticles capped with both ligands in an approximately 1:1 ratio (confirmed by XPS, **Supplementary Fig. 43**). This ETL mimics the bulk ligand environment of the graded structure, but also without a doping profile (**Supplementary Fig. 42c**).

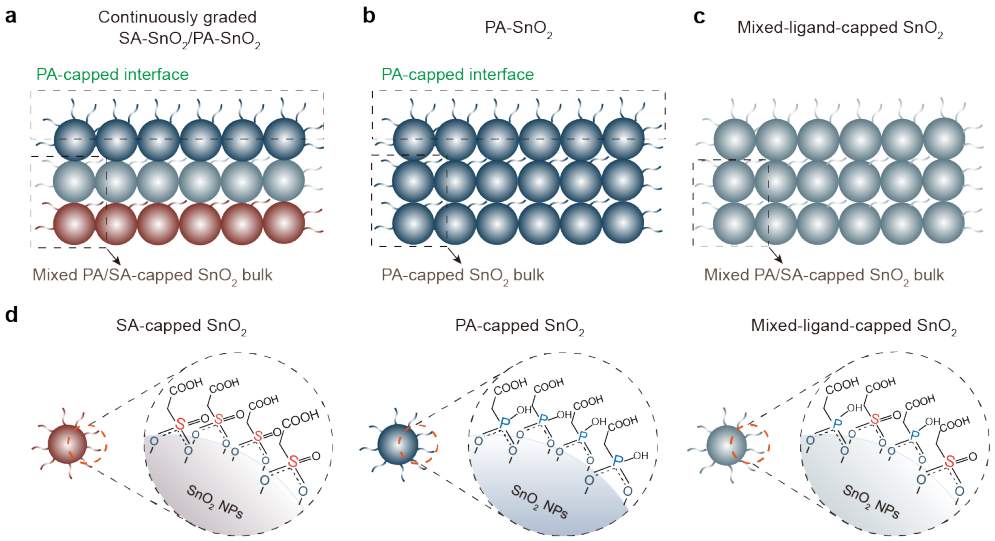

Supplementary Fig. 42 a, **b**, **c**, Schematic diagrams of SnO_2 films with different ligands capping at the interface or within the bulk. **d**, Schematic diagrams of different ligands capped SnO_2 nanoparticles.

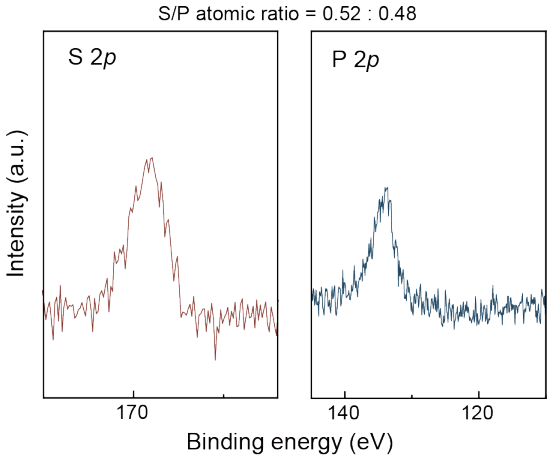

Supplementary Fig. 43 XPS spectra of S 2*p* and P 2*p* signal for mixed-ligand-capped SnO_2.

To gain deeper insight on carrier extraction dynamics, we compared the graded ETL to the homogeneous PA-capped ETL (which has identical interface chemistry). As shown in **Supplementary Fig. 44**, TRPL measurements revealed a faster electron extraction at the graded interface. To further quantify these differences, the electron-transfer rate (k_{ET}) and extraction efficiency (η_{ET}) for PA-capped interface were also calculated and were summarized in **Supplementary Table 4**. The results confirmed that the graded interface consistently maintained superior charge transfer characteristics, with higher electron-transfer rate (k_{ET}) and extraction efficiency (η_{ET}) than that of PA-capped ETL (2.5×10^7 s^{-1} and 98.72%). This indicated that the graded

doping modifies the internal electric field profile, facilitating more efficient drift of photogenerated electrons toward the ETL and reducing interfacial accumulation, a benefit that pure chemical passivation cannot provide.

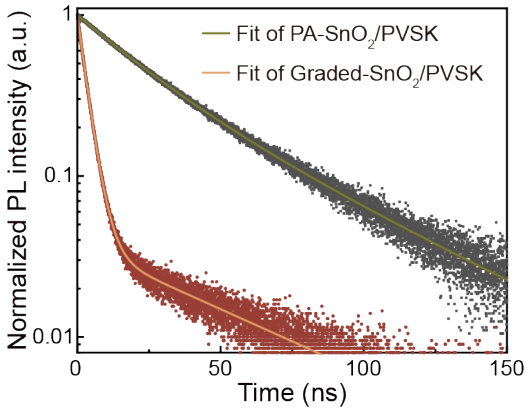

Supplementary Fig. 44 TRPL spectra of PA-SnO_2/perovskite and graded SnO_2/perovskite stacks.

Then we compared device performance to verify whether the continuously graded structure can outperform the homogeneous ligand capping analogue. Accordingly, photovoltaic devices were fabricated using these control ETLs and benchmarked against the continuously graded ETL device.

Pure PA-capped SnO_2 device: Despite exhibiting nearly identical band alignment and interfacial passivating chemistry at the perovskite/ETL interface to the graded device (**Supplementary Fig. 45a**), its performance remained notably lower, particularly in open circuit voltage (V_{oc}) (26.60% vs. 27.64%), consistent with the SCAPS-1D simulation results (**Supplementary Note 6**). This disparity directly implicated the graded doping as the origin of the enhanced V_{oc}.

Mixed PA/SA-capped SnO_2 device: Although this ETL possesses similar bulk ligand composition, the device achieved only 26.64% efficiency, which is markedly below the 27.64% of the graded device (**Supplementary Fig. 45b**).

Collectively, these comparisons showed that neither interfacial passivation alone (pure PA) nor bulk ligand mixing alone (mixed PA/SA) can reproduce the performance gain; the graded distribution is essential.

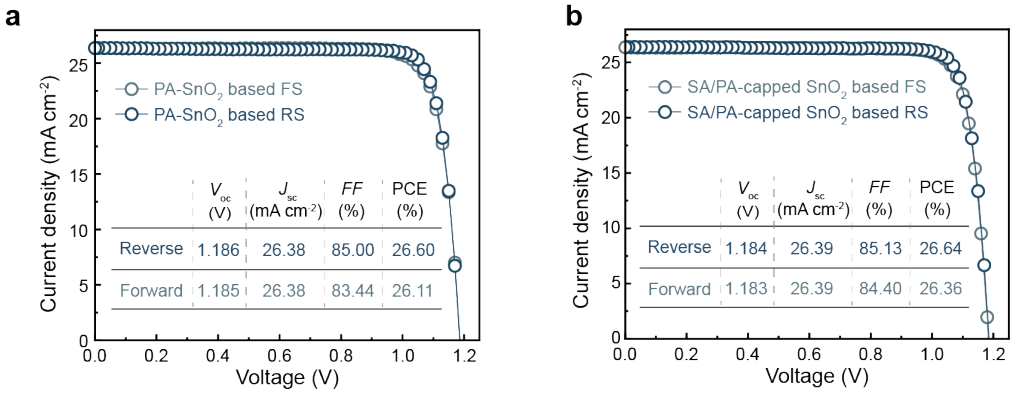

Supplementary Fig. 45 *J-V* curves for PSCs based on PA-SnO_2 ETL (**a**) and mixed-ligand-capped SnO_2 ETL (**b**), respectively.

3. Third, to elaborate the physical and optoelectronic merits of continuously graded-doped SnO_2 ETLs over a discrete bilayer counterpart (non-continuously graded structure), we constructed a well-defined bilayer ETL *via* sequential deposition of SA-SnO_2 (0.3 mM SA-ligand for 3 h) and PA-SnO_2 (0.15 mM PA-ligand for 3 h), guided by the deposition time-thickness profile (**Supplementary Fig. 46a**). The process yielded a total film thickness of ~43 nm, which was comparable to that of the continuously graded-doped SnO_2 ETL, with a uniform and compact surface morphology (**Supplementary Figs. 46b**, **c**).

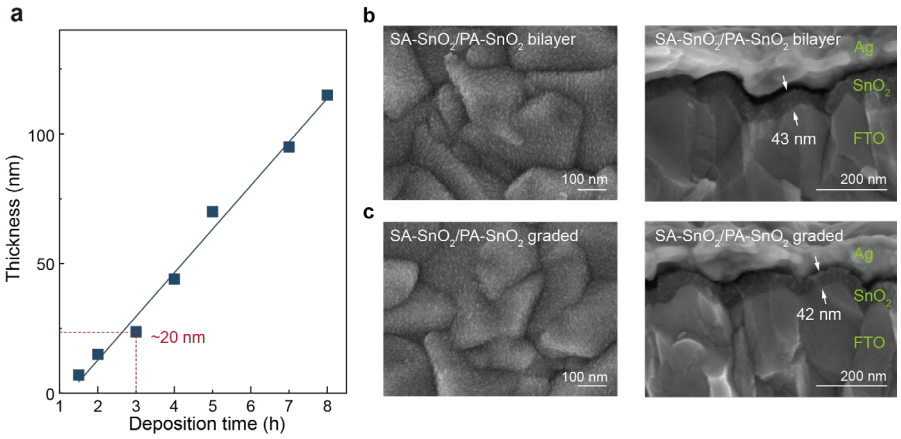

Supplementary Fig. 46 a, SnO_2 films thickness versus deposition time profile. SEM and cross-sectional SEM images of SA-SnO_2/PA-SnO_2 bilayer film (**b**) and SA-SnO_2/PA-SnO_2 continuously graded film (**c**).

Then, TRPL measurements were conducted on SA-SnO_2/PA-SnO_2

bilayer/perovskite and SA-SnO_2/PA-SnO_2 continuously graded ETL/perovskite interfaces (**Supplementary Fig. 47a**). The carrier decay kinetics, quantified by the differential lifetime $\tau = -(d\ln(\phi(t))/dt)^{-1}$, revealed a faster rise of τ at early times for the graded-doped ETL relative to the bilayer control, directly indicating more efficient electron extraction (**Supplementary Fig. 47b**). Quantitative analysis of the k_{ET} and η_{ET} further corroborated this trend (**Supplementary Table 4**): both k_{ET} and η_{ET} for the bilayer SnO_2/perovskite interface (3.69×10^7 s^{-1} and 99.13%) were distinctly lower than those of the graded-doped ETL/perovskite interface (4.18×10^7 s^{-1} and 99.19%). These enhancements were attributed to improved field-driven charge extraction, which effectively reduced carrier accumulation and nonradiative recombination at the buried interface. Consistently, higher PLQY and QFLS values were observed for the graded ETL/perovskite stack, approaching those of the neat perovskite film (**Supplementary Fig. 47c**).

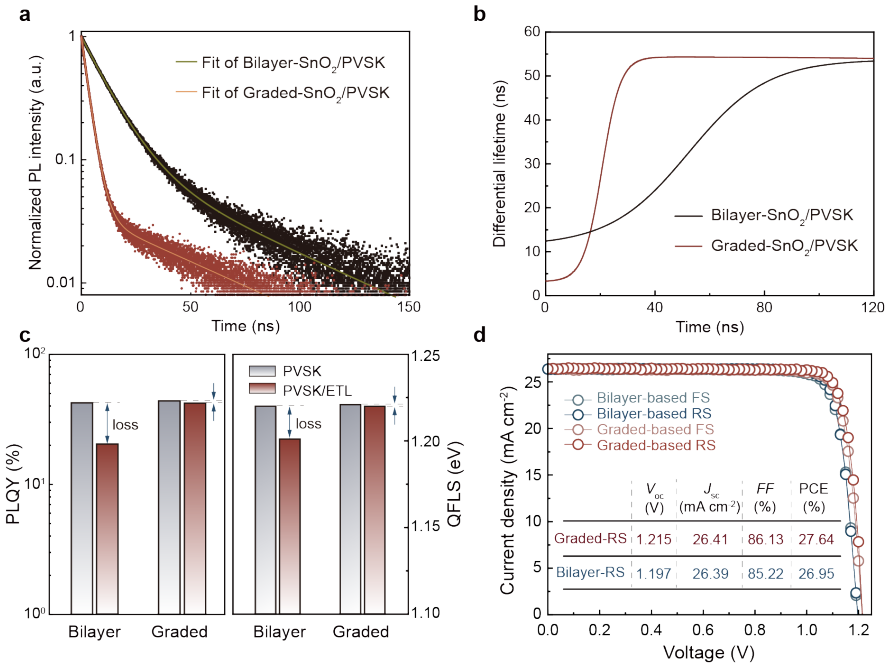

Supplementary Fig. 47 TRPL spectra (**a**) and differential lifetimes (**b**) of bilayer-SnO_2/perovskite and graded-SnO_2/perovskite stacks. **c**, PLQY spectra and corresponding QFLS for perovskite stacked with bilayer-SnO_2 and graded-doped SnO_2 ETLs. **d**, *J-V* curves for n-i-p devices based on bilayer and graded-SnO_2 ETLs.

Consequently, in agreement with the SCAPS-1D simulation results

(**Supplementary Note 6**), the continuously graded-doped SnO_2 ETL delivered superior performance, with PCE increasing from 26.95% (bilayer) to 27.64% (**Supplementary Fig. 47d**), indicating clear performance advantage for the graded architecture.

4. Finally, to validate the uniqueness of the LCB strategy based on controlled hydrolysis of DMPA, we constructed a graded SnO_2 using an alternative approach by continuously introducing PA ligands during the intermediate stage of the CBD process (denoted IPA-SnO_2). As shown in **Supplementary Fig. 48a**, TOF-SIMS confirmed that this IPA strategy can also produce a graded SnO_2 profile. However, this approach introduces two critical limitations that compromise device performance. First, the continuous introduction of PA ligands during deposition led to severe particle aggregation, resulting in a rough and inhomogeneous film morphology (**Supplementary Fig. 49a**). Second, TOF-SIMS mapping revealed pronounced in-plane heterogeneity of the PO_2^- distribution (**Supplementary Fig. 49c**), indicating that the PA ligands were not uniformly incorporated across the substrate. These morphological and compositional inhomogeneities translate directly into degraded photovoltaic performance: devices fabricated with the IPA-SnO_2 ETL exhibited a PCE (reverse scanning, 26.40%) loss of up to 1.24% compared to the LCB-SnO_2 counterparts (reverse scanning, 27.64%) (**Supplementary Fig. 48b**).

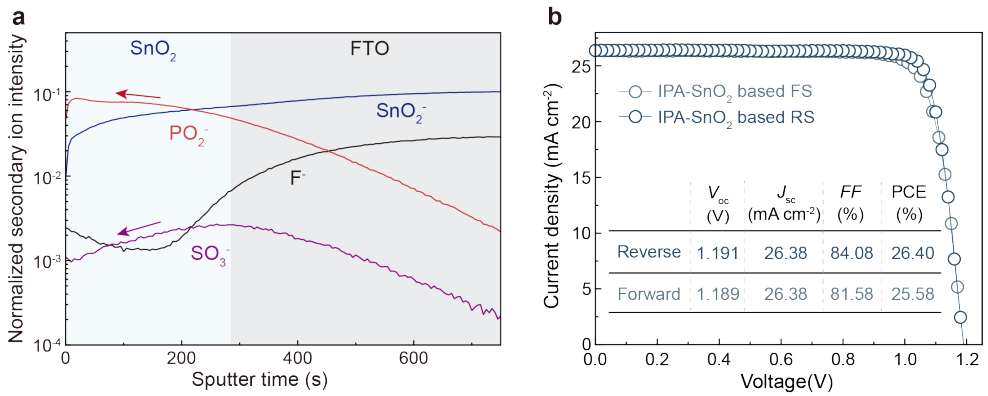

Supplementary Fig. 48 a, TOF-SIMS depth profiles of PO_2^- from PA and SO_3^- from SA in IPA-SnO_2 film. **b**, *J-V* curves for n-i-p devices based on IPA-SnO_2 ETL.

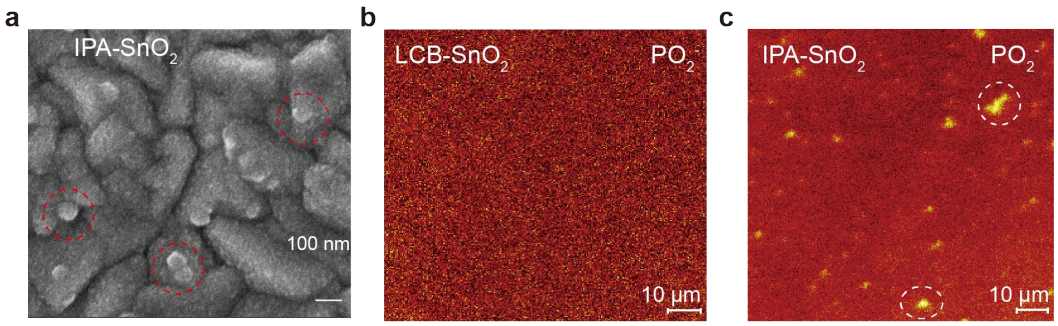

Supplementary Fig. 49 a, SEM image of IPA-SnO_2 film. **b**, **c**, TOF-SIMS maps of PO_2^- for LCB-SnO_2 film and IPA-SnO_2 film, respectively.

Transient reflectance (TR) analysis

To quantitatively describe the variation in carrier density under different photoexcitation conditions, a one-dimensional diffusion equation was employed[14,15].

$$\frac{\partial N(x,t)}{\partial t} = D\frac{\partial^2 N(x,t)}{\partial x^2} - \frac{N(x,t)}{\tau_B} \quad 9$$

where $N(x,t)$ is the carrier density as a function of depth (x) and time (t), D is the ambipolar diffusion coefficient and τ_B is the carrier lifetime in the bulk.

Carrier generation by the pulse is assumed to be instantaneous compared to the timescale of carrier diffusion. The initial carrier concentration at the film surface was thus calculated as following:

$$N(x,0) = N_0 \exp(-\alpha x) \quad 10$$

where N_0 is the initial carrier density, defined as $N_0 = \alpha\ (1 - R)\ J_0$, with J_0 representing the pump fluence and R is the reflectance at the pump-photon energy.

For polycrystalline samples, the film thickness no longer exceeds the optical penetration depth plus the carrier diffusion length. Under such conditions, the boundary conditions are described as

$$\frac{\partial N(x,t)}{\partial x}\Big|_{x=0} = \frac{SEV}{D}N(0,t) \quad 11$$

$$\frac{\partial N(x,t)}{\partial x}\Big|_{x=M} = -\frac{SRV}{D}N(L,t) \quad 12$$

where M is the film thickness, SEV and SRV were the surface extraction velocity and surface recombination velocity, respectively. Furthermore, bulk carrier recombination was considered negligible for time delays shorter than 5 ns. The numerical solution $N(0,t)$ was incorporated into a global fitting procedure to determine the optimal value of the surface extraction velocity (SEV). The extracted D value was 2.1 ± 0.2 $cm^2\ s^{-1}$, and the SRV value was 1,190 ± 200 $cm\ s^{-1}$, determined as the intrinsic SRV on the perovskite surfaces that were not in contact with the ETL.

Supplementary Note 11 | Device certification.

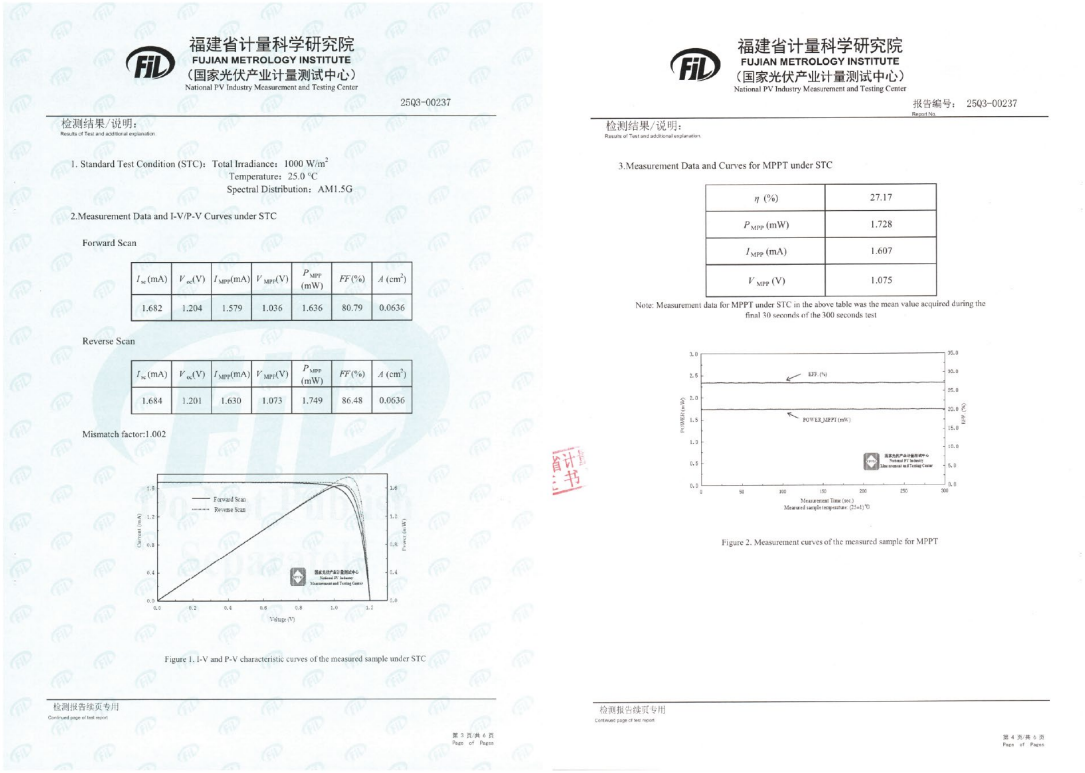

福建省计量科学研究院
FUJIAN METROLOGY INSTITUTE
（国家光伏产业计量测试中心）
National PV Industry Measurement and Testing Center

2503-00237

检测结果/说明：

1. Standard Test Condition (STC)：Total Irradiance：1000 W/m²
Temperature：25.0 °C
Spectral Distribution：AM1.5G

2.Measurement Data and I-V/P-V Curves under STC

Forward Scan

I_{sc} (mA)	V_{oc} (V)	I_{MPP} (mA)	V_{MPP} (V)	P_{MPP} (mW)	FF (%)	A (cm²)
1.682	1.204	1.579	1.036	1.636	80.79	0.0636

Reverse Scan

I_{sc} (mA)	V_{oc} (V)	I_{MPP} (mA)	V_{MPP} (V)	P_{MPP} (mW)	FF (%)	A (cm²)
1.684	1.201	1.630	1.073	1.749	86.48	0.0636

Mismatch factor:1.002

Figure 1. I-V and P-V characteristic curves of the measured sample under STC

检测报告续页专用

福建省计量科学研究院
FUJIAN METROLOGY INSTITUTE
（国家光伏产业计量测试中心）
National PV Industry Measurement and Testing Center

报告编号： 2503-00237

检测结果/说明：

3.Measurement Data and Curves for MPPT under STC

η (%)	27.17
P_{MPP} (mW)	1.728
I_{MPP} (mA)	1.607
V_{MPP} (V)	1.075

Note: Measurement data for MPPT under STC in the above table was the mean value acquired during the final 30 seconds of the 300 seconds test

Figure 2. Measurement curves of the measured sample for MPPT

检测报告续页专用

Supplementary Fig. 50 Device certification. Independent certification was performed by the National PV Industry Measurement and Testing Center (NPVM), China. The certified stabilized power output (SPO) and reverse-scan PCE of the device with a continuously graded-doped SnO_2 ETL reached 27.17% and 27.50%, respectively.

Supplementary Table 5. Summary of certified steady-state PCE > 25% for PSCs in both n-i-p and p-i-n configuration.

Device structure	E_g (eV)	V_{oc} (V)	*FF* (%)	J_{SC} (mA cm^{-2})	Steady-state PCE (%)	V_{oc} loss (mV)	N (%)	*Ref.*
n-i-p	**1.51**	**1.201**	**86.48**	**26.48**	**27.17**	**309**	**93.01**	**This work**
p-i-n	1.51	1.189	86.75	26.61	27.18	321	92.37	*Science* 2025, 390, 638[16]
p-i-n	1.53	1.185	86.75	26.18	26.15	345	90.57	*Nature* 2025, 646, 95[17]
p-i-n	1.52	1.200	84.31	25.90	25.9	320	89.86	*Science* 2025, 387, 186[18]
p-i-n	1.55	1.197	85.17	26.21	26.14	353	88.40	*Nat. Photon.* 2025, 19, 1070[19]
p-i-n	1.56	1.193	84.59	26.20	25.85	377	86.14	*Nat. Mater.* 2025, 24, 1265[20]
n-i-p	1.53	1.180	84.78	25.58	25.02	350	88.14	*Nat. Energy* 2025, 10, 1226[21]
n-i-p	1.50	1.179	84.25	26.40	25.8	321	89.69	*Nat. Photon.* 2025, 19, 985[22]
n-i-p	1.53	1.164	86.52	26.35	25.72	366	88.73	*Nat. Photon.* 2025, 19, 701[23]
n-i-p	1.53	1.196	83.5	25.65	25.65	339	89.87	*Nat. Energy* 2025, 10, 774[10]
p-i-n	1.53	1.185	83.70	26.51	26.15	345	87.39	*Nature* 2025, 642, 78[2]
p-i-n	1.53	1.192	84.11	26.47	26.54	338	88.33	*Nature* 2024, 632, 536[24]
p-i-n	1.53	1.174	85.20	26.13	26.15	356	88.13	*Science* 2024, 384, 189[25]
n-i-p	1.55	1.170	82.63	27.23	25.94	380	83.83	*Nat. Energy* 2024, 9, 1506[26]
n-i-p	1.53	1.186	84.98	26.43	25.94	344	88.80	*Nature* 2024, 635, 82[9]
n-i-p	1.54	1.191	84.20	26.04	26.0	349	87.65	*Nat. Commun.* 2024, 15, 8620[6]
p-i-n	1.53	1.153	82.45	26.50	25.16	377	83.76	*Nature* 2023, 624, 557[27]
p-i-n	1.53	1.183	81.20	26.24	25.20	347	84.63	*Science,* 2023, 382, 1399[28]
p-i-n	1.50	1.170	84.50	26.20	25.11	330	89.27	*Science* 2023, 382, 810[29]
n-i-p	1.51	1.179	84.60	25.80	25.73	331	89.32	*Nature* 2023, 616, 724[13]
n-i-p	1.53	1.174	82.00	26.38	25.39	356	84.8	Science 2022, 375, 302[30]
n-i-p	1.51	1.1885	83.20	25.74	25.49	324	88.5	*Nature* 2021, 598, 444[31]
n-i-p	1.54	1.181	80.58	25.14	25.17	359	87.5	*Nature* 2021, 590, 587[32]

*N (%) represents the V_{oc} and *FF* product relative to the SQ limits of its corresponding band gap.

Process scalability.

We offer a perspective on the practical utility of the CBD process from the following considerations. To demonstrate the compatibility of the LCB-enabled CBD strategy, we fabricated large-area devices, including 1 cm^2 solar cells and 5 × 5 cm^2 solar modules.

By employing the continuously graded-doped CBD SnO_2 ETL, we achieved high-performance large-area PSCs, delivering power conversion efficiencies of 25.79% for a 1 cm^2 device and 23.33% for a 5 × 5 cm^2 module (**Extended Data Fig. 2**), thereby highlighting the scalability and practical potential of this approach.

Notably, the substantial efficiency gains, arising from the superior conformality and optimized band alignment of the CBD-derived ETL, offset the moderately increased deposition time, resulting in a favorable trade-off for high-value applications such as building-integrated photovoltaics and flexible modules.

Supplementary Note 12 | Device stability.

PSCs based on the continuously graded-doped SnO_2 ETL were subjected to a series of rigorous stability tests, including damp-heat testing under the ISOS-D-3 protocol (85 °C and 85% RH) and thermal cycling testing following the IEC 61215:2021 standard (between -40 °C and 85 °C), using poly[bis(4-phenyl) (2,4,6-trimethylphenyl)amine] (PTAA) as the HTL. Prior to testing, all devices were encapsulated with a UV-curable resin and cover glass, thereby ensuring that the observed degradation arises from intrinsic material instability rather than extrinsic environmental ingress.

As shown in **Supplementary Fig. 51**, the devices retained 90% of their initial efficiency after 956 h under damp-heat testing. Furthermore, 88% of the initial efficiency was maintained after 200 cycles between -40 °C and 85 °C (**Supplementary Fig. 52**). These performances were comparable to those of state-of-the-art photovoltaic devices, as summarized in **Supplementary Table 6** and **Supplementary Table 7**, collectively underscored the robustness of our LCB-SnO_2 architecture and its suitability for practical applications.

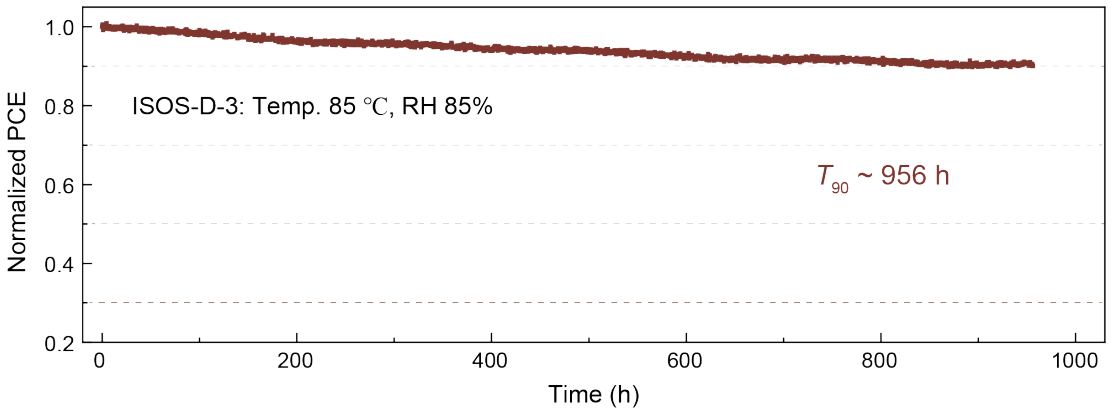

Supplementary Fig. 51 Damp-heat stability of the continuously graded-doped SnO_2-based encapsulated PSCs under ISOS-D-3 protocols (85 ℃, 85% relative humidity).

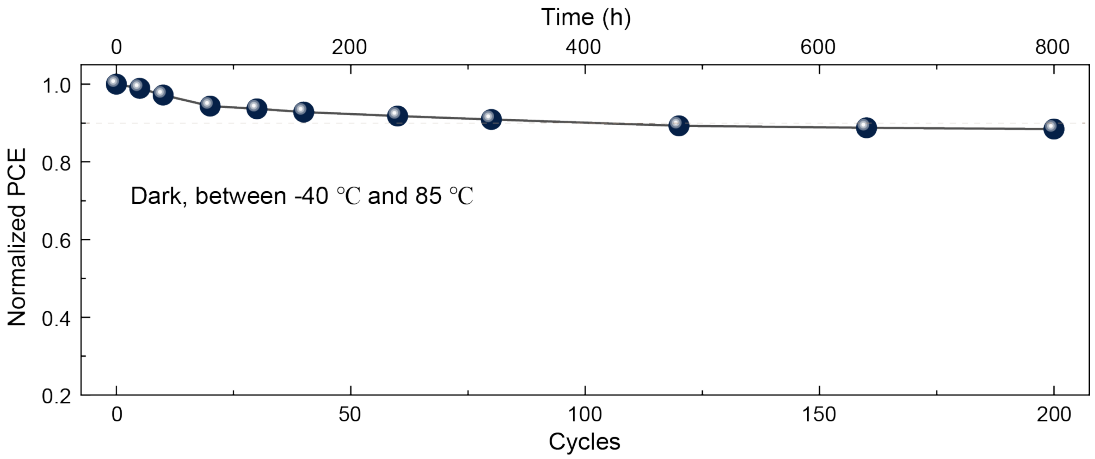

Supplementary Fig. 52 Thermal-cycling stability between -40 ℃ and 85 ℃ of the continuously graded-doped SnO_2-based encapsulated PSCs.

To gain deeper mechanistic insight into the robustness stability of the SnO_2 ETL, we conducted *ab initio* molecular dynamics (AIMD) simulations for ligand-bound SnO_2 at 358 *K* (85 ℃). The simulations were run for 8 ps to ensure thermodynamic equilibration and to capture the dynamic behavior of ligand-surface interactions under elevated temperature. As shown in **Supplementary Fig. 53**, both SA and PA ligands remained firmly anchored to the SnO_2 surface throughout the simulation trajectory after equilibration, with no desorption events observed. The AIMD results provided atomic-scale evidence that the strong ligand-substrate binding confers high intrinsic resistance to thermal and humid stress.

To experimentally validate these insights, we further performed TOF-SIMS measurements on encapsulated graded-SnO_2/perovskite films subjected to aging at 85 °C and 85% RH under continuous illumination for up to 500 h to assess the stability of the SnO_2 ETL. As shown in **Supplementary Fig. 54**, the aged sample (500 h) exhibited no obvious changes compared to the fresh film. Critically, no PO_2^- or SO_3^- signals were detectable within the perovskite layer after aging, and their graded distribution within the SnO_2 ETL was fully preserved. These results confirmed that the ligands remain robustly bound to SnO_2, with no desorption or interlayer diffusion, in good agreement with the AIMD results.

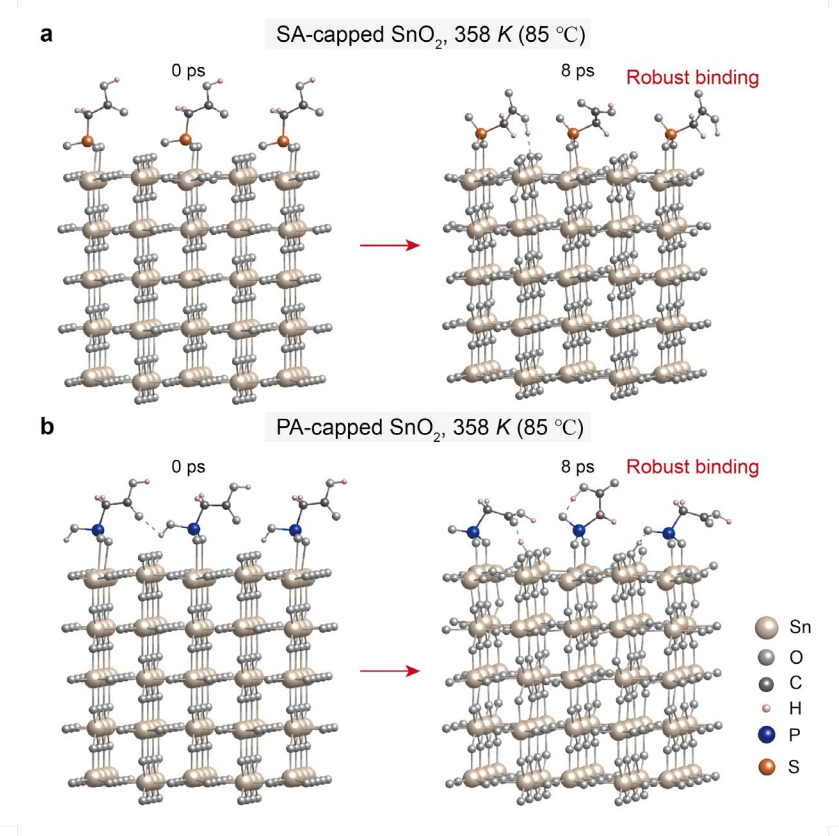

Supplementary Fig. 53 AIMD simulations of ligands binding for SA (**a**) and PA (**b**) under 358 K (85 ℃).

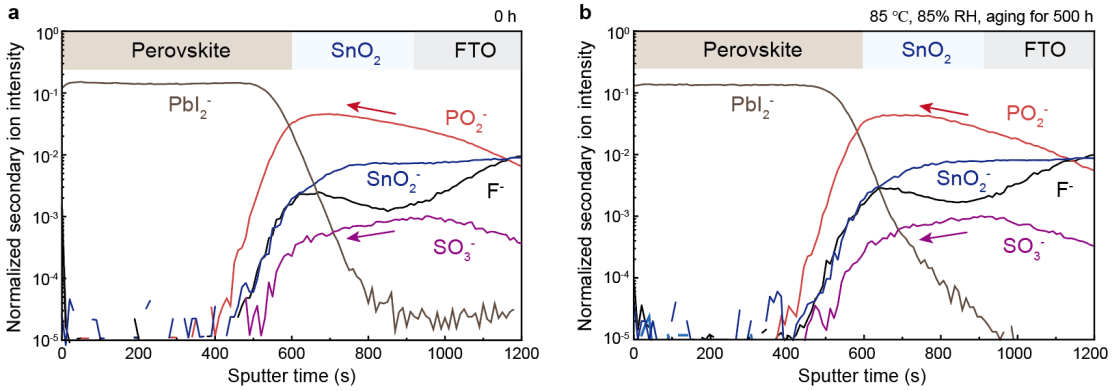

Supplementary Fig. 54 TOF-SIMS depth profiles of SnO_2/perovskite film with aging treatments for 0 h (**a**) and 500 h (**b**) under 85 °C and 85% RH, respectively.

Supplementary Table 6. Summary of the reported operating stability of n-i-p PSCs under damp-heat conditions (ISOS-D-3 protocol).

ISOS protocol	Relative Humidity	Temperature	Lifetime	Ref.
ISOS-D-3	**~85%**	**85 ℃**	**T_{90} = 956 h**	**This work**
ISOS-D-3	~85%	85 ℃	T_{86} = 900 h	*Nat. Energy* 2025, 10, 774[10]
ISOS-D-3	~85%	85 ℃	T_{92} = 600 h	*Science* 2024, 384, 878[33]

Supplementary Table 7. Summary of the reported device's operating stability under thermal-cycling conditions in n-i-p PSCs.

Temperature	Cycles	PCE retention (%)	Ref.
-40~85 ℃	**200**	**T_{88} = 800 h**	**This work**
-40~85 ℃	200	T_{80} > 1200 h	*Science* 2024, 384, 878[33]
-40~85 ℃	200	90%	*Angew. Chem. Int. Ed.* 2025, 64, e202421063[41]

Reference

1. Ma, Y. et al. Enhancing hole-conductor-free, printable mesoscopic perovskite solar cells through post-fabrication treatment via electrophilic reaction. *Nat. Energy* (2025) doi.org/10.1038/s41560-025-01823-8.
2. Lin, Y. et al. A Nd@C_{82}-polymer interface for efficient and stable perovskite solar cells. *Nature* **642**, 78-84 (2025).
3. Xing, G. et al. Long-range balanced electron- and hole-transport lengths in organic-inorganic $CH_3NH_3PbI_3$. *Science* **342**, 344-347 (2013).
4. Stranks, S. D. et al. Electron-hole diffusion lengths exceeding 1 micrometer in an organometal trihalide perovskite absorber. *Science* **342**, 341-344 (2013).
5. Jiang, Q. et al. Enhanced electron extraction using SnO_2 for high-efficiency planar-structure $HC(NH_2)_2PbI_3$-based perovskite solar cells. *Nat. Energy*, **2**, 16177 (2017).
6. Qu, Z. et al. Enhanced charge carrier transport and defects mitigation of passivation layer for efficient perovskite solar cells. *Nat. Commun.* **15**, 8620 (2024).
7. Lu, Y. et al. Rational design of a chemical bath deposition based tin oxide electron-transport layer for perovskite photovoltaics. *Adv. Mater.* **35**, e2304168 (2023).
8. Dong, J. et al. Carrier management through electrode and electron-selective layer engineering for 10.70% efficiency antimony selenosulfide solar cells. *Nat. Energy* **10**, 857-868 (2025).
9. Li, S. et al. High-efficiency and thermally stable $FACsPbI_3$ perovskite photovoltaics. *Nature* **635**, 82-88 (2024).
10. Seo, G. et al. Efficient and luminescent perovskite solar cells using defect-suppressed SnO_2 via excess ligand strategy. *Nat. Energy* **10**, 774-784 (2025).
11. Kavan, L. et al. Ultrathin buffer layers of SnO_2 by atomic layer deposition: perfect blocking function and thermal stability. *J. Phys. Chem. C* **121**, 342-350 (2017).
12. Yu, B. et al. Impermeable atomic layer deposition for sputtering buffer layer in efficient semi-transparent and tandem solar cells via activating unreactive substrate. *Adv. Mater.* **35**, 2202447 (2023).
13. Park, J. et al., Controlled growth of perovskite layers with volatile alkylammonium chlorides. *Nature* **616**, 724-730 (2023).
14. Gong, S. et al. A hot carrier perovskite solar cell with efficiency exceeding 27% enabled by ultrafast hot hole transfer with phthalocyanine derivatives. *Energy & Environ. Sci.* **17**, 5080 (2024).
15. Yang, Y. et al. Top and bottom surfaces limit carrier lifetime in lead iodide perovskite films. *Nat. Energy* **2**, 16207 (2017).

16. Zhuang, X. et al. Homogenized chlorine distribution for >27% power conversion efficiency in perovskite solar cells. *Science* **390**, 638-642 (2025).
17. Jiang, W. et al. Toughened self-assembled monolayers for durable perovskite solar cells. *Nature* **646**, 95-101 (2025).
18. Zai, H. et al. Wafer-scale monolayer MoS_2 film integration for stable, efficient perovskite solar cells. *Science* **387**, 186-192 (2025).
19. Gao, D. et al. High-efficiency perovskite solar cells enabled by suppressing intermolecular aggregation in hole-selective contacts. *Nat. Photon.* **19**, 1070-1077 (2025).
20. Luo, C. et al. Engineering bonding sites enables uniform and robust self-assembled monolayer for stable perovskite solar cells. *Nat. Mater.* **24**, 1265-1272 (2025).
21. Zhao, J. et al. Impact of lithium dopants in hole-transporting layers on perovskite solar cell stability under day-night cycling. *Nat. Energy* **10**, 1226-1236 (2025).
22. Wang, Y. et al. Solvent-assisted reaction for spontaneous defect passivation in perovskite solar cells. *Nat. Photon.* **19**, 985-991 (2025).
23. Tang, X. et al. Enhancing the efficiency and stability of perovskite solar cells via a polymer heterointerface bridge. *Nat. Photon.* **19**, 701-708 (2025).
24. Liu, S. et al. Buried interface molecular hybrid for inverted perovskite solar cells. *Nature* **632**, 536-542 (2024).
25. Chen, H. et al. Improved charge extraction in inverted perovskite solar cells with dual-site-binding ligands. *Science* **384**, 189-193 (2024).
26. Li, Q. et al. Harmonizing the bilateral bond strength of the interfacial molecule in perovskite solar cells. *Nat. Energy* **9**, 1506-1516 (2024).
27. Liang, Z. et al. Homogenizing out-of-plane cation composition in perovskite solar cells. *Nature* **624**, 557-563 (2023).
28. Yu, S. et al. Homogenized NiO_x nanoparticles for improved hole transport in inverted perovskite solar cells. *Science* **382**, 1399-1404 (2023).
29. Liu, C. et al. Bimolecularly passivated interface enables efficient and stable inverted perovskite solar cells. *Science* **382**, 810-815 (2023).
30. Kim, M. et al. Conformal quantum dot-SnO_2 layers as electron transporters for efficient perovskite solar cells. *Science* **375**, 302-306 (2022).
31. Min, H. et al. Perovskite solar cells with atomically coherent interlayers on SnO_2 electrodes. *Nature* **598**, 444-450 (2021).
32. Yoo, J.J. et al. Efficient perovskite solar cells via improved carrier management. *Nature* **590**, 587-593 (2021).
33. Duan, T. et al. Chiral-structured heterointerfaces enable durable perovskite solar cells. *Science* **384**, 878-884 (2024).
34. Hu, J. et al. Molecular press annealing enables robust perovskite solar cells. *Science* **391**,164-170 (2026).

35. Shi, P. et al. Oriented nucleation in formamidinium perovskite for photovoltaics. *Nature* **620**, 323-327 (2023).
36. Zhang, T. et al. Ion-modulated radical doping of spiro-OMeTAD for more efficient and stable perovskite solar cells. *Science* **377**, 495-501 (2022).
37. Wang, T. et al. Transporting holes stably under iodide invasion in efficient perovskite solar cells. *Science* **377**, 1227-1232 (2022).
38. Huang, Z. et al. Anion-π interactions suppress phase impurities in $FAPbI_3$ solar cells. *Nature* **623**, 531-537 (2023).
39. Bai, Y. et al. Initializing film homogeneity to retard phase segregation for stable perovskite solar cells. *Science* **378**, 747-754 (2022).
40. Zhao, Y. et al. Inactive $(PbI_2)_2RbCl$ stabilizes perovskite films for efficient solar cells. *Science* **377**, 531-534 (2022).
41. Li, Z. et al. In-situ cross-linked polymers for enhanced thermal cycling stability in flexible perovskite solar cells. *Angew. Chem. Int. Ed.* **64**, e202421063 (2025).